J. Fluid Mech. (2007), *vol.* 571, *pp.* 281–326.
doi:10.1017/S0022112006003351 Printed in the United Kingdom

Coherent structure in a turbulent jet via a vector implementation of the proper orthogonal decomposition

By M. O. IQBAL AND F. O. THOMAS

Center for Flow Physics and Control, Department of Aerospace and Mechanical Engineering, University of Notre Dame, Notre Dame, IN 46556, USA

(Received 26 July 2005 and in revised form 11 July 2006)

The coherent structure in the near-field of an axisymmetric turbulent jet at a Reynolds number of 3.8×10^5 and Mach number of 0.3 is experimentally characterized by a vector implementation of the proper orthogonal decomposition (POD). The POD eigenfunctions and associated eigenvalues are extracted at several selected streamwise locations in the initial region. The focus on the near-field is motivated by its importance in numerous technical applications. Results show a rapid energy convergence with POD mode number. Examination of the relative energy contained in the combined azimuthal and radial components of the POD modes reveals that it is comparable to that in the streamwise component. The streamwise evolution of the eigenvalue spectra is characterized by a remarkable variation in the azimuthal mode number energy distribution, leading to the dominance of azimuthal mode $m = 1$ beyond the end of the jet core. In contrast, a scalar implementation using only the streamwise component shows the dominance of mode $m = 2$ which is consistent with previous scalar implementations of the POD. For a given azimuthal mode number, the eigenvalue spectra exhibit a broad peak which occurs at a constant value of Strouhal number based on local shear layer momentum thickness and local jet maximum velocity. The phase information required for a local reconstruction of the jet structure is obtained by projecting the POD eigenmodes onto instantaneous realizations of the flow at fixed streamwise locations. The instantaneous realizations are obtained by utilizing cross-stream arrays of multi-sensor probes in conjunction with linear stochastic estimation (LSE). Results clearly show the local dynamic behaviour of each component of the jet structure.

1. Introduction

1.1. *Motivation and background*

In this paper the large-scale structure in the near field of a high-Reynolds-number axisymmetric jet is studied experimentally by an implementation of the proper orthogonal decomposition (POD) which utilizes all three fluctuating velocity components. As was the case in Gordeyev & Thomas (2000), a summation of the most energetic POD modes is considered synonymous with the term 'large-scale structure'. This work is focused on extracting POD eigenfunctions and their associated eigenvalues at selected streamwise locations throughout the jet initial region. The focus on the near field of the axisymmetric jet is motivated by its importance in many technical applications such as propulsion systems, chemical

mixers and jet noise. For example, one application of considerable interest involves the identification, characterization and control of coherent structures in high-bypass-ratio aircraft engines for the purpose of noise reduction. A more complete understanding of the large-scale structure in the simpler axisymmetric jet shear layer investigated here is prerequisite to achieving this goal in the multiple-shear-layer engine flow.

Numerous experiments have shown that the near-field evolution of the axisymmetric jet is a consequence of large-scale, spatially coherent vortical motions which are initiated via an inviscid, inflectional instability mechanism. These coherent structures play an important role in determining macro-characteristics of the flow such as mean mass, momentum and scalar transport as well as aerodynamic noise generation. A review of early attempts to characterize the coherent motions in the near field of the axisymmetric jet is presented in Thomas (1991) and Bonnet & Delville (2001).

Bonnet & Delville (1996) provide a comprehensive review of a variety of experimental techniques that have been developed in order to extract coherent structures from turbulent shear flows. So-called conditional techniques involve sampling the flow only during those time intervals in which a dynamically significant event that is associated with the coherent structure is occurring. While useful, such techniques may suffer from a lack of objectivity in the sense that one must have a predetermined notion of the structure topology and its effect on the instantaneous flow. In contrast, the proper orthogonal decomposition (POD) proposed by Lumley (1967, 1970) for the investigation of inhomogeneous turbulent shear flows is an example of a non-conditional technique that is based on the two-point velocity correlation. The mathematical basis of the POD is the Karhunen–Loéve expansion as described in Karhunen (1946) and Loéve (1955). The analysis of turbulent shear flows by the POD is the subject of a comprehensive review by Berkooz, Holmes & Lumley (1993) and the monograph by Holmes, Lumley & Berkooz (1996). The POD objectively extracts a complete, orthogonal set of spatial eigenfunctions (i.e. 'modes') from the measured second-order correlation function. These POD eigenmodes provide an optimal basis for expansion of the flow in the sense that energy convergence is more rapid than for any other basis. It is reasonable, therefore, to associate a summation of the most energetic POD modes with the large-scale, energy-containing structure in the jet.

As pointed out by Lumley (1967, 1970), the POD eigenfunctions are known only to within an arbitrary function of phase. The phase information required for reconstruction of the coherent structure in physical space is obtained by projection of the POD modes back onto instantaneous realizations of the flow field. This allows temporal phase coefficients for each mode to be determined. These phase coefficients embody the mode's dynamic behaviour. In order to preserve phase information in an experimental context, rakes or meshes containing multiple synchronized probes are typically utilized. A very useful review of such multi-point measurement techniques in turbulent flow is presented by Glauser & George (1992). Alternatively, Galerkin projection of the dominant POD modes onto the appropriately simplified version of the Navier–Stokes equations for the flow provides a finite system of ODEs that allows the flow field dynamics to be examined within the framework of well-defined dynamical systems and bifurcation theory. Examples of this approach are Aubry *et al.* (1988) in the near-wall turbulent boundary layer and Ukeiley *et al.* (2001) in the planar mixing layer.

While this investigation is certainly not the first to apply the POD to characterize axisymmetric turbulent jet flow structure, it is the first to report a full vector implementation utilizing all three fluctuating velocity components. Comparison of the results of the current study to previous scalar implementations will reveal significant

differences in the underlying flow physics. A brief review of previous POD work in the axisymmetric jet follows and will provide the framework in which the contributions of the current work may be placed.

1.2. *Previous applications of the POD in the axisymmetric jet*

The first implementation of the POD in the near field of an axisymmetric jet is reported by Glauser, Leib & George (1987). Seven single-sensor hot-wires aligned in the radial direction were used to obtain cross-spectra between measured streamwise fluctuating velocity components at a location three nozzle diameters downstream of the jet exit. This scalar implementation of the POD demonstrated a rapid energy convergence with mode number. The first POD mode was found to contain nearly 40 % of the turbulent energy, whereas the first three POD modes captured nearly all the resolved turbulent kinetic energy. This work was subsequently extended by Glauser & George (1987) by adding a second rake of seven straight wires at the same streamwise location that permitted obtaining cross-spectra involving both radial and azimuthal probe separations. The second rake was sequentially positioned azimuthally relative to the stationary rake in 12^o increments. The authors examined the energy contained in the first POD mode for azimuthal mode number $m = 0$ relative to that in all combined azimuthal modes in order to determine whether the axisymmetric mode is dominant. They found that this energy ratio was approximately 0.23 suggesting that a few higher azimuthal modes should be included in the definition of the coherent structure. A conceptual model for turbulence production in the axisymmetric shear layer was described by Glauser (1987) which involves the interaction between two adjacent vortex ring structures shed from the nozzle lip.

In a different implementation of the POD, Arndt, Long & Glauser (1997) demonstrate that the fluctuating pressure signal measured at the outer edge of the axisymmetric jet is hydrodynamic in nature and can be used to infer large-scale flow structure embedded within the jet. Using multiple microphones positioned at the edge of the jet and separated in the streamwise direction, they present a unique scalar implementation of the POD based on measured pressure fluctuations. In contrast to the previously cited studies, the streamwise coordinate was treated as inhomogeneous. It was found that the phase speed of each POD eigenmode is 0.58 U_j. Using the shot-noise decomposition, dynamic events such as vortex pairings and triplings were inferred.

In an effort to examine the dynamics of the axisymmetric jet shear layer and thereby complement the earlier results of Glauser (1987), Citriniti & George (2000) used a polar array of 138 synchronized straight wire probes (only the streamwise velocity component was measured) at a fixed location three diameters downstream of the nozzle exit. The array was used to acquire simultaneous single-component realizations of the flow at multiple locations in the r–θ crossflow plane onto which the POD eigenfunction basis was projected. In this manner the local temporal dynamics of the flow field was obtained. It was shown that only five azimuthal modes ($m = 0, 3, 4, 5, 6$) are required to faithfully represent the local dynamics of the large-scale structure. The study showed that the local jet structure is characterized by azimuthally coherent 'volcano-like' events near the jet potential core. Evidence was also found that suggested the presence of streamwise-aligned, counter-rotating vortices connecting the adjacent azimuthally coherent structures.

Extending previous POD work to the compressible axisymmetric jet, Ukeiley & Seiner (1998) were the first to examine the streamwise evolution of POD eigenspectra. Their investigation focused on the streamwise range of $4 \leqslant x/D \leqslant 12$ in a jet with

Mach number $M = 0.85$. That study was motivated, in part, by a desire to explore the mechanism of subsonic jet noise production. The authors used a rake of six X-wires aligned in the radial direction at a single azimuthal location and obtained cross-spectra involving both the streamwise and radial fluctuating velocity components. As was the case in previous low-speed jet studies, the first POD mode captured approximately 40 % of the resolved kinetic energy while the first five modes captured almost 90 %. Ukeiley, Seiner & Ponton (1999) subsequently extended the previously cited study by adding a second rake of X-wires for computing cross-spectra between the streamwise and radial fluctuating components in the $r-\theta$ cross-stream plane. In this manner the azimuthal dependence of the POD eigenspectra were also obtained. Three Mach numbers were considered ($M = 0.3, 0.6, 0.85$) though results were only presented for $M = 0.3$ and $M = 0.6$. It was found that the azimuthal mode $m = 7$ dominates the flow field at $x/D = 4$, whereas this peak shifts towards lower azimuthal mode number ($m = 4$) as the jet approaches $x/D = 8$. Comparison of results for the two cases presented showed no strong Mach-number dependence.

Jung, Gamard & George (2004) and Gamard, Jung & George (2004) used essentially the same hot-wire array as Citriniti & George (2000) to investigate the evolution of modal energy content in the near field of the jet over the streamwise range $2 \leqslant x/D \leqslant 6$ and in the far field ($20 \leqslant x/D \leqslant 69$). As in the work by Citriniti & George only the streamwise-fluctuating component was measured. The experiments showed that the POD eigenspectra varied significantly in the downstream direction. They demonstrated a progressive shift of the dominant azimuthal mode from $m = 0$ at $x/D = 3$ to azimuthal mode $m = 2$ by $x/D = 6$. In the far field of the axisymmetric jet ($x/D = 20$ to 69) they showed that the azimuthal mode $m = 2$ continues to dominate the flow in apparent contradiction to the widely held belief that azimuthal mode $m = 1$ should be dominant (e.g. Cohen & Wygnanski, 1987). The authors also demonstrate that the properly normalized eigenspectra do not depend on the downstream distance in the similarity region. This is analogous to the self-similar scaling of POD eigenfunctions and eigenvalues observed in the far field of the planar jet by Gordeyev & Thomas (2000).

1.3. *Objectives*

The objective of the present investigation is to experimentally characterize the coherent structure in the near field of a high-Reynolds-number axisymmetric jet via a full, three-component implementation of the POD. The POD eigenfunctions and associated eigenvalues are experimentally extracted in a manner similar to that employed by Delville *et al.* (1999) in the planar mixing layer and Gordeyev & Thomas (2000) in the planar jet. This will provide an objective description of the time-averaged coherent structure in the axisymmetric jet flow field in a mixed Fourier–physical domain. In order to examine the jet coherent structure in physical space, the POD eigenfunctions are subsequently projected onto instantaneous cross-stream realizations of the jet flow field obtained at several selected streamwise locations by following the procedure of Gordeyev & Thomas (2002). The realizations used for the POD projection are acquired by means of a sparse cross-stream array of X-wires used in conjunction with the linear stochastic estimation (LSE) technique. The remainder of the paper is organized as follows. In § 2 the experimental facility is described and the axisymmetric jet flow field validated. In § 3 the experimental implementation of the POD is described. Results characterizing the streamwise evolution of the jet large-scale structure are presented in § 4. Finally, the results are summarized and compared with earlier studies in the discussion of § 5.

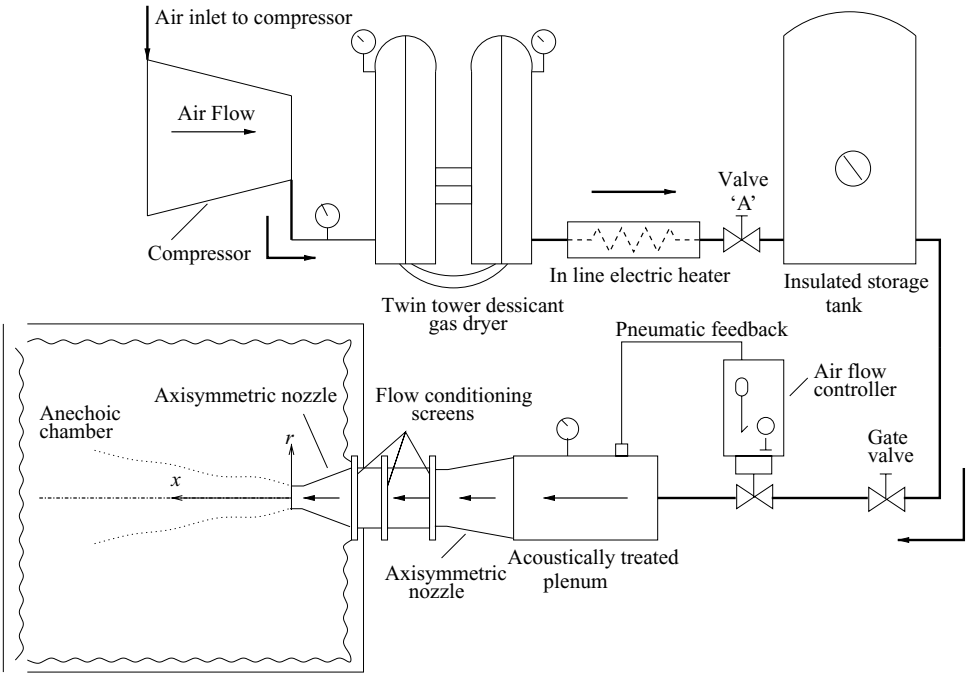

FIGURE 1. Schematic of the high-speed jet facility.

2. Experimental facility and basic flow field characteristics

2.1. *Jet flow field facility*

The experimental facility is shown schematically in figure 1. Readers interested in details of the facility are referred to Iqbal (2006). Here only essential aspects are provided.

The facility is of the blowdown type and jet flow is initiated by opening a pneumatically controlled gate valve. During tank discharge, the stagnation pressure in the plenum chamber upstream of the nozzle assembly is maintained at a constant, preset value by a pressure controller with pneumatic feedback control. The pressure controller maintains the plenum pressure to within $\pm 0.5\,\%$ of the preset value. The plenum chamber is lined with acoustic absorbent foam in order to minimize the propagation of noise from upstream piping to the jet nozzle assembly.

The jet discharges from an axisymmetric nozzle with fifth-order polynomial wall contour and zero-derivative end conditions. The exit diameter of the nozzle is $D = 5.06\,\text{cm}$. The facility is capable of producing a steady, heated air jet with core turbulence intensity levels of less than $u_{rms}/U_j < 0.1\,\%$ (where the subscript *rms* denotes a root-mean-square value) and exit Mach numbers of up to 1.0. For the exit Mach number $M = 0.3$ used for this study, the system is capable of providing a run time of approximately 25 min.

The flow discharges from the nozzle exit into a large anechoic chamber which provides an anechoic free-field environment with a demonstrated low-frequency cutoff of approximately 400 Hz (see Walker & Thomas 1997). Although not the focus of this paper, the chamber is sufficiently large to make both near-and far-field acoustic measurements. An additional advantage of performing the flow field measurements in the anechoic chamber is the elimination of unintentional facility-dependent acoustic

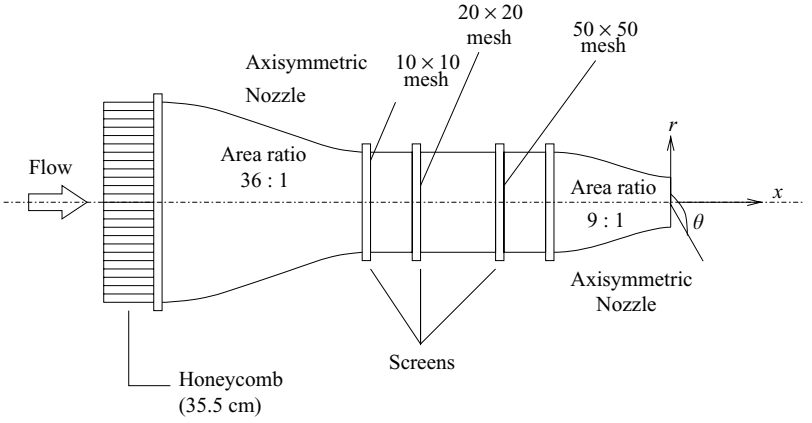

FIGURE 2. Schematic of the axisymmetric nozzle and upstream attachments.

forcing due to propagation of reflected sound waves to the nozzle lip. Owing to the long acoustic wavelengths in relation to the jet diameter, such forcing will be azimuthally coherent at the jet lip and can therefore excite the axisymmetric mode (see Gutmark & Ho 1983 and Tam 1986). More will be said of this in the results section. It should also be noted that care was taken in the design of the anechoic chamber to avoid any significant overpressure by venting sufficient flow to the outside.

In this paper x will denote the streamwise spatial coordinate, which is typically made non-dimensional by nozzle exit diameter D. The other two spatial coordinates for the flow are in the radial, r, and azimuthal, θ, directions. The origin of the coordinate axes is chosen to be the centre point of the nozzle exit plane as shown in figure 2. The velocity components corresponding to the x, r, θ coordinates are denoted as u, v, and w, respectively.

2.2. *Characterization of the basic flow field*

Unless otherwise noted, for the measurements presented in this study, the jet facility was operated with a nozzle exit velocity of $U_j = 110\,\mathrm{m\,s^{-1}}$ which corresponds to an exit Mach number of $M = 0.3$ and a Reynolds number, $Re_D = 380\,000$ (based on nozzle exit diameter). The jet was not heated. Figure 3 presents measured jet mean velocity profiles obtained at several streamwise locations. The mean streamwise velocity, U, is normalized by the local maximum velocity $U_{max}(x/D)$ and is plotted against the radial coordinate r normalized by local jet mean velocity half-width, $b(x)$. The half-width is defined as the radial location at which the local jet mean velocity falls to one-half its centreline value. This figure shows that the mean velocity profile initially possesses a 'top-hat' shape which is indicative of a uniform potential core flow bounded by a thin axisymmetric shear layer. The initial jet shear layer momentum thickness was determined to be $\theta_0 = 0.051\,\mathrm{mm}$, or $\theta_0/D = 0.001$. The mean velocity variation across the shear layer is approximated well by a hyperbolic tangent profile shape. The jet shear layer widens with streamwise distance and engulfs the irrotational core flow near $x/D = 5.0$. Figure 3 shows that the jet mean velocity profile subsequently approaches a state of mean velocity similarity by $x/D = 8.0$. Figure 4 summarizes the streamwise evolution of both the jet width, $2b(x)/D$, and the centreline mean velocity, U_{max}/U_j. The jet centreline mean velocity is nearly constant until the end of the jet potential core near $x/D = 5.0$ but decays farther downstream. Measurements show an apparent asymptotic mean velocity decay rate

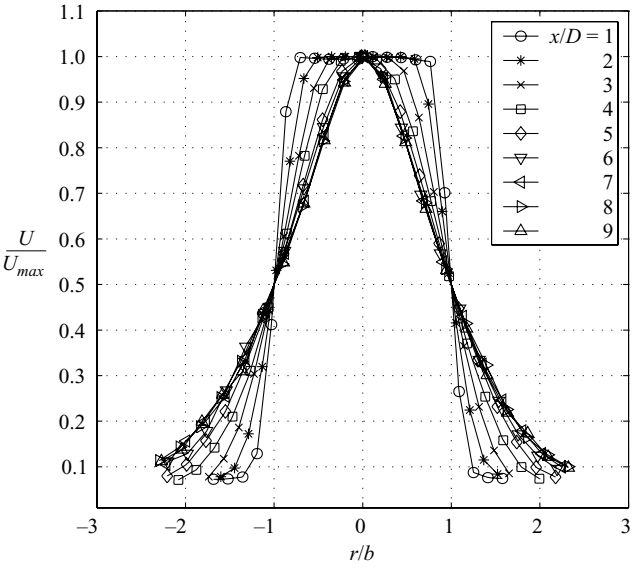

FIGURE 3. Scaled jet mean velocity profiles at several streamwise locations.

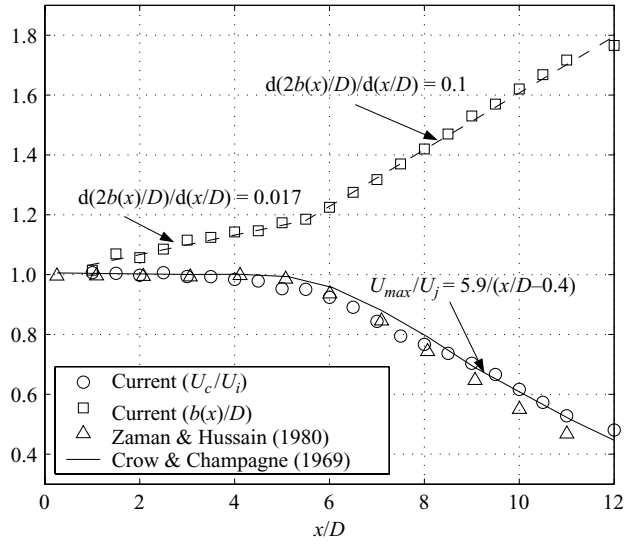

FIGURE 4. Streamwise variation of jet width $2b(x)/D$ and jet centreline velocity U_{max}/U_j.

given by $(U_{max}/U_j) = 5.9/(x/D - 0.4)$. The jet spreading rate is initially small but approaches an asymptotic value of $d(2b/D)/d(x/D) = 0.1$ beyond the tip of the jet core. As shown in figure 4, these values are in excellent agreement with the results obtained in other axisymmetric jet facilities by Zaman & Hussain (1980), Crow & Champagne (1971), and Hussein, Capp & George (1994).

It is well-known that profiles of second-order turbulence statistics generally require longer streamwise distances to exhibit similarity than does the mean flow (e.g. Wygnanski & Fiedler 1969 and Gutmark & Wygnanski 1976). This is observed in the streamwise-component turbulence intensity profiles obtained at representative

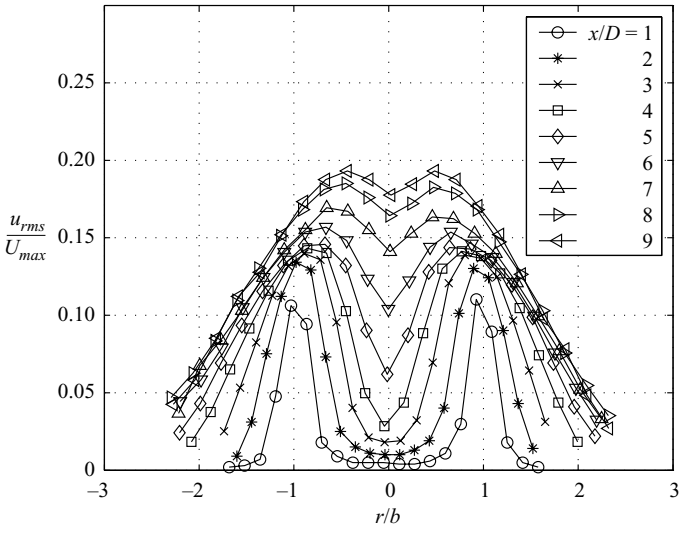

FIGURE 5. Profiles of u_{rms}/U_{max} at various x/D locations.

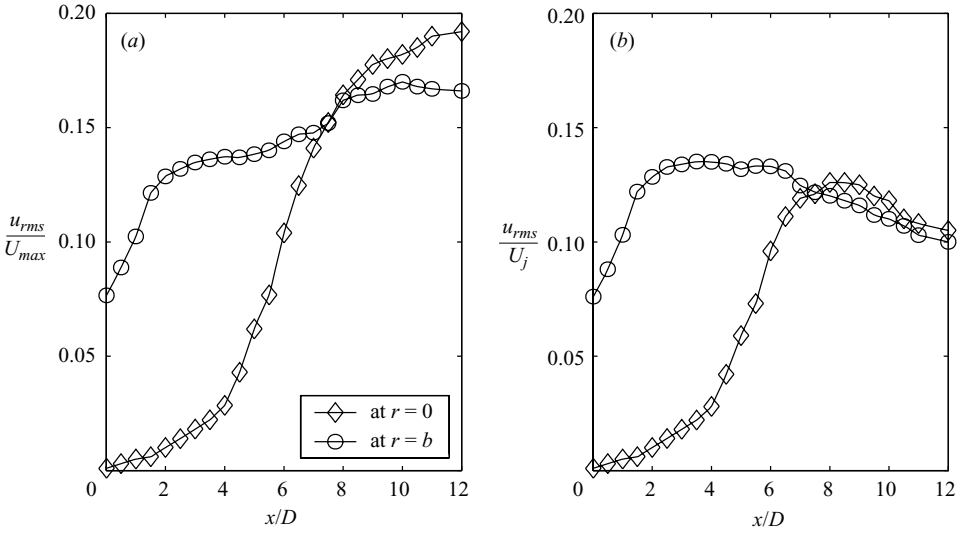

FIGURE 6. Streamwise evolution of $u_{rms}|_{r=0}$ and $u_{rms}|_{r=b}$.

x/D locations as shown in figure 5. No collapse of the scaled r.m.s. velocity profiles is observed. Figure 6(a) presents the streamwise evolution of both the jet centreline turbulence intensity $u_{rms}|_{r=0}/U_{max}$ and that obtained in the middle of the jet shear layer ($r/b = 1$). Figure 6(b) presents the same centreline and shear layer u_{rms} scaled with the jet exit velocity, U_j. This figure shows that in the shear layer ($r/b = 1$), u_{rms}/U_j saturates near $x/D = 3.5$ and near $x/D = 8.5$ on the jet centreline. These measurements are in good general agreement with the above-cited experiments.

Standard fast Fourier analysis techniques were used to characterize the spectral content of streamwise velocity fluctuations in the jet. The spectra shown in figure 7 are ensemble averaged over 200 blocks with $N = 2048$ points per block with a Nyquist frequency of 5 kHz. Figure 7 presents u-component autospectra obtained on the jet

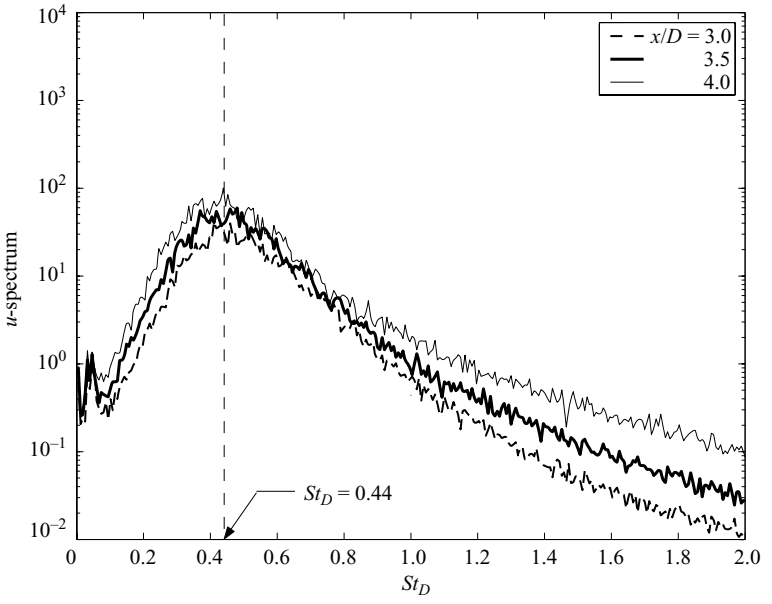

FIGURE 7. u-component autospectra at the centreline of the jet for various x/D locations.

centreline at several x/D locations upstream of the tip of the jet core. Here the frequency is expressed in terms of the Strouhal number, $St_D = fD/U_j$. As shown in figure 7, the spectra each exhibit a well-defined peak near $St_D = 0.42$–0.45 which is a manifestation of the jet column instability. As noted by Thomas (1991), St_D values reported in the literature vary widely (0.25–0.85). However, as noted by Kibens (1981), for $D/2\theta_0 > 120$, St_D is nearly constant with a value of approximately $St_D \approx 0.44$. In the current study, $D/2\theta_0 = 496$.

Autospectra were also obtained in the axisymmetric jet shear layer in order to characterize the development of the shear layer instability frequency. For these measurements the Nyquist frequency was increased to 50 kHz. Block size and the number of ensembles were 2048 and 400, respectively. The shear layer spectra were acquired at several streamwise locations, each at a radial location where the r.m.s. of the streamwise fluctuating velocity reaches a local maximum. Representative shear layer spectra are plotted in figure 8. As indicated, the fundamental shear layer instability frequency occurs at a Strouhal number (based on initial shear layer momentum thickness) of $St_{\theta_0} = 0.0126$. This value compares well with the results of Zaman & Hussain (1981) and Drubka (1981) who measured values of 0.012 and 0.013, respectively. This confirms that the nascent jet facility is quite 'clean' in terms of being free from facility-dependent forcing of the shear layer. The fundamental instability is observed to saturate by $x/D = 0.1$ and this corresponds to approximately 2.4 fundamental instability wavelengths downstream of the nozzle exit. Soon after that, a broad subharmonic peak grows and overtakes the fundamental. This is a manifestation of a parametric resonance with the mean flow as described by Monkewitz (1988) and Ho & Huang (1982). As expected, the subharmonic dominates the shear layer spectrum at $x/D = 0.11$ as shown in figure 8.

From shear layer spectra measured farther downstream (not presented here) it was noted that for $x/D > 1.75$ the spectral distributions were completely broadband with a well defined $-5/3$ roll-off suggesting establishment of turbulent flow conditions.

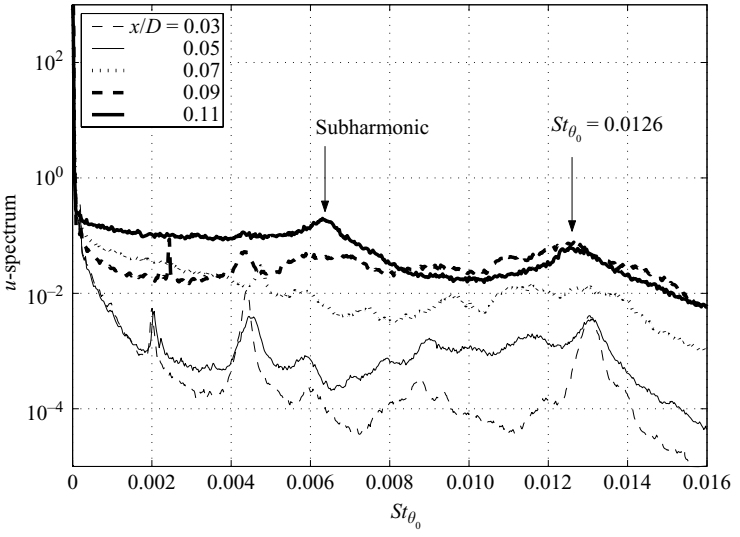

FIGURE 8. Nascent jet shear layer u-component autospectra for various x/D locations.

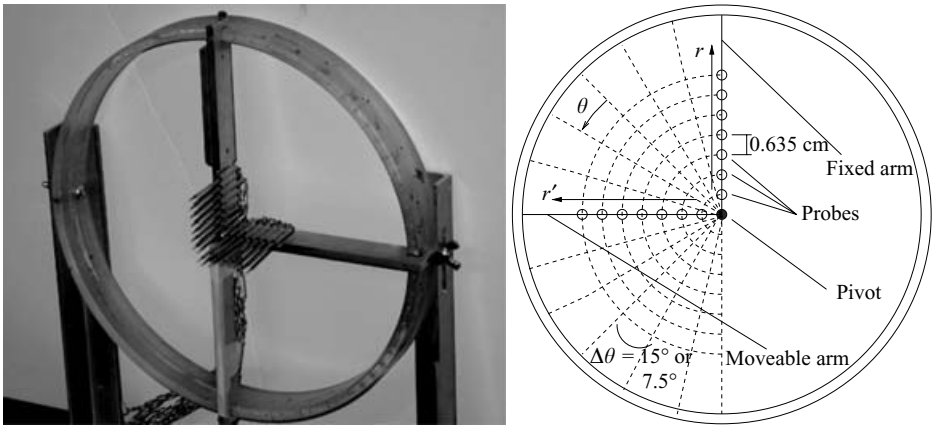

FIGURE 9. Schematic and photograph of the twin rake arrangement.

Hence one may safely conclude that by the first POD measurement station ($x/D = 3$) the jet shear layer was fully turbulent.

2.3. *Multi-point velocity measurements*

As described in detail in a subsequent section, the experimental implementation of the POD requires the measurement of the velocity cross-correlation tensor at selected x/D locations. The cross-correlation tensor for a fixed x-location is defined as

$$R_{\alpha\beta}(r, r', \theta, \theta', t, t') = \langle u_\alpha(r, \theta, t) u_\beta(r', \theta', t') \rangle, \tag{2.1}$$

where $\langle . \rangle$ denotes an ensemble average and Greek subscripts (α and β) denote fluctuating velocity components u, v, or w. The process of obtaining the cross-correlation tensor is expedited by the use of cross-stream rakes of X-wire probes which allow one to simultaneously acquire velocity–time histories at multiple cross-stream locations. Probe locations at the first and second rake are denoted as (r, θ) and (r', θ'), respectively, as shown in figure 9 which provides a schematic of the rake

geometry. Hence the velocity measurement $u_\alpha(r, \theta, t)$ corresponds to the α component at the first rake and $u_\beta(r', \theta', t)$ corresponds to the β component at the second rake. Note that the X-wire probes are capable of measuring either $(\alpha = u, \beta = v)$ or $(\alpha = u, \beta = w)$ simultaneously depending upon the orientation of the probe sensors. Because the flow is stationary in time, t, and is assumed homogeneous in the azimuthal direction, θ, the cross-correlation matrix $R_{\alpha\beta}(r, r', \theta, \theta', t, t')$ actually depends only on the relative coordinates $\Delta\theta \equiv \theta - \theta'$ and $\tau \equiv t - t'$.

Figure 9 shows both a schematic of the cross-stream measurement grid and a corresponding photograph of one of the two rake set-ups used for the POD measurements. Fourteen miniature X-wire probes fabricated by Auspex Corporation (type AHWX-100) are used. These X-wire probes have a 0.9 mm spacing between the two probe sensors and a sensor wire length of 0.8 mm. There are seven probes in each rake, equally spaced radially, with one rake fixed and the other moveable in the azimuthal direction. The pivot point of the moveable rake is positioned at the centreline of the jet, i.e. at $r = 0$. The radial separation of the probes on each rake is $\Delta r = 0.635$ cm. Depending upon which twin rake set-up was used, the moveable rake was positioned at intervals of either $\Delta\theta = 15^\circ$ or $\Delta\theta = 7.5^\circ$ in order to form the measurement grid shown in figure 9. The rake assembly is mounted on a table with a provision to position it at streamwise locations given by $3.0 \leqslant x/D \leqslant 12$.

The required 28-channels of constant-temperature hot-wire anemometry and associated anti-alias filters were fabricated in-house. The dynamic response of the transducers was found to be flat to 50 kHz. The anti-alias filtered output voltages from the hot-wire sensors were simultaneously sampled and digitized by means of a 36-channel data acquisition system made by MicroStar Laboratories (data acquisition processor DAP 3400a and simultaneous sampling board MSXB028). This system is capable of simultaneously sampling the 28 hot-wire output voltages at rates up to 50 kHz with no detectable phase lag between the channels. Additional input channels are used to record the instantaneous jet exit velocity and temperature from a differential pressure transducer and thermocouple, respectively. The digital data are logged to an internal drive in binary format on a laboratory personal computer for post-processing.

The X-wires were calibrated in the axisymmetric jet facility by means of a removable rotating table which simultaneously placed all of the X-wires into the potential core near the nozzle exit of the round jet. The table pivots the probes about an axis passing through the centre of each X-wire array and thereby allows one to set a given yaw angle between the probe axis and the oncoming uniform flow. Since density fluctuations were negligible, the probes were calibrated directly in terms of velocity. During calibration the speed of the jet was set to six different values within the range from 0 to 135 m s^{-1} (the upper value corresponds to $M = 0.4$) as measured by a Pitot probe connected to a differential pressure transducer. The X-wire probe angle with respect to the oncoming flow was set to eleven different values within the range of -45° to $+45^\circ$. The anemometer bridge voltage from each hot-wire sensor was recorded for each velocity–flow angle combination. These data were used to create a look-up table to compute velocity vectors from the voltages measured during the experiment. The look-up table procedure used in this study is similar to that described in Chu (1993), Ukeiley & Glauser (1995) and Gordeyev & Thomas (2000).

Alignment of the rake arrangement with respect to the axis of the jet is obviously important for proper characterization of the jet POD modes. It was also important to verify that the jet developed symmetrically in θ. It is clear from measurements like those shown in figures 3 and 5 that the jet development is radially symmetric. In addition, azimuthal symmetry was examined by considering the azimuthal variation

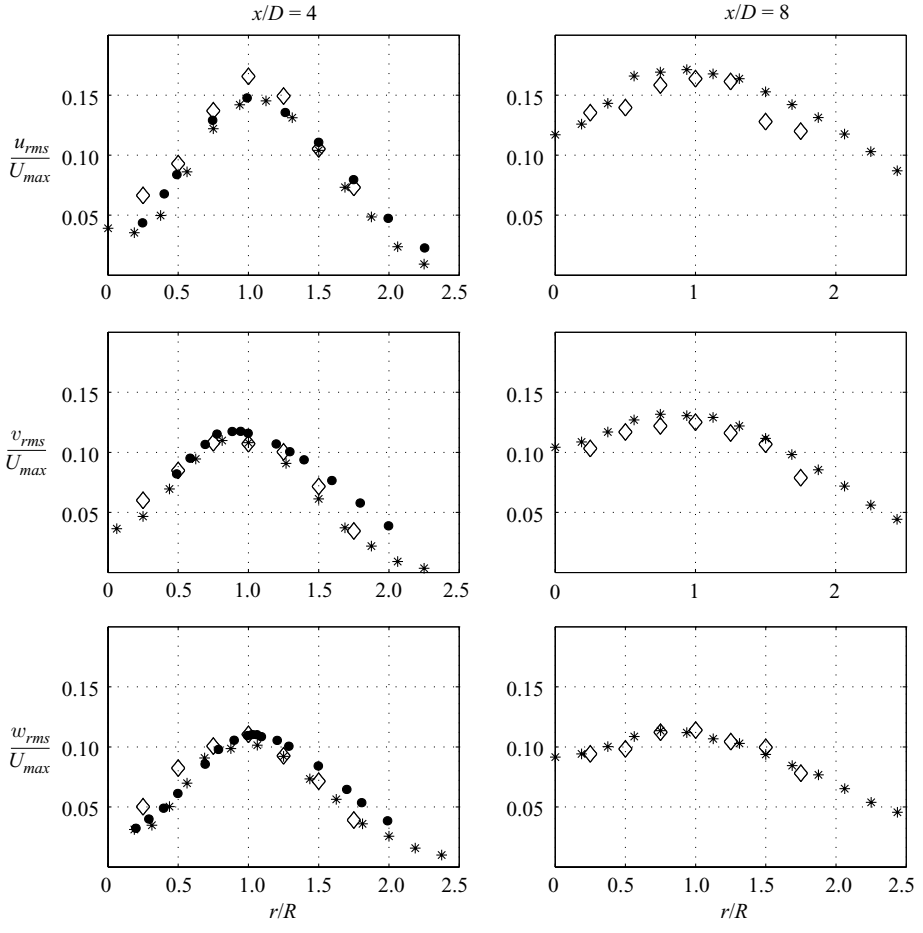

FIGURE 10. Comparison of r.m.s. fluctuating velocity at $x/D = 4$ and 8: $\diamond$, the current rake-based data; *, the data obtained by traversing a single X-wire probe; ● data reported by Bradshaw *et al.* (1964).

of the mean streamwise velocity component, $U(r, \theta)$ and the normal turbulent stresses, $\langle u^2 \rangle$, $\langle v^2 \rangle$, and $\langle w^2 \rangle$ as obtained with the rake arrangement at representative radial locations in the (r, θ)-plane and for $0 \leqslant \theta \leqslant 2\pi$. The measurements were performed for $3 \leqslant x/D \leqslant 12$. Results clearly showed that both the mean flow and normal turbulent stress components exhibited complete azimuthal symmetry at each streamwise location. This ensured that the proper alignment of the rake arrangement with the jet axis had been achieved.

In order to ensure that the presence of the rake arrangement does not adversely affect measurements made in the jet, a quantitative comparison is made between cross-stream profiles of all three r.m.s. fluctuating velocity components obtained with the rake-arrangement shown in figure 9 and by traversing a single multi-sensor probe across the jet under identical experimental conditions. Figure 10 presents the comparison of cross-stream profiles of the three r.m.s. turbulence intensity components. The radial coordinate is normalized by the nozzle radius, R. The comparison is shown at two representative streamwise locations. At $x/D = 4$ the current measurements are also compared with the published data obtained by

Bradshaw, Ferriss & Johnson (1964) under similar experimental conditions but in a different facility. The agreement between the current measurements utilizing the rake and the traverse of a single multi-sensor probe confirms that the rake has no significant effect on the fluctuating velocity measurements. Comparison to the measurements of Bradshaw *et al.* (1964) serves to further validate the three-component turbulence data obtained from the jet flow field facility.

3. Experimental implementation of the POD

In this section, the experimental procedure by which the POD eigenmodes and eigenvalues are obtained from the axisymmetric jet flow is described. The method is similar in approach to that successfully implemented by Delville *et al.* (1999) in the planar mixing layer and by Gordeyev & Thomas (2000) in the planar jet.

3.1. *Basic procedure*

As described previously, the twin rake arrangement of X-wires shown in figure 9 is used to acquire the fluctuating velocity $u_\alpha(r, \theta, t)$. Since time is a homogeneous coordinate, the cross-spectral matrix, $S_{\alpha\beta}(r, r', \Delta\theta, f)$ may be obtained from a temporal Fourier transform of the velocity correlation matrix $R_{\alpha\beta}$,

$$S_{\alpha\beta}(r, r', \Delta\theta, f) = \int R_{\alpha\beta}(r, r', \Delta\theta, \tau)\mathrm{e}^{-2\pi i f\tau}\,\mathrm{d}\tau \tag{3.1}$$

Alternatively, the cross-spectral matrix $S_{\alpha\beta}(r, r', \Delta\theta, f)$ may be obtained directly from Fourier transformation of the individual velocity–time histories as described in Bendat & Piersol (1986), and this is the approach taken in this investigation. This gives the equivalent relation,

$$S_{\alpha\beta}(r, r', \Delta\theta, f) = \lim_{T\to\infty} \frac{1}{T}\langle \hat{u}^*_\alpha(r, \theta, f)\hat{u}_\beta(r', \theta + \Delta\theta, f)\rangle, \tag{3.2}$$

where $\hat{u}_\alpha(r, \theta, f) \equiv \int_0^T u_\alpha(r, \theta, t)\exp(-2\pi\mathrm{i} f t)\,\mathrm{d}t$ denotes Fourier transformation of the velocity vector for each block, T is the total time duration of the data block and the asterisk denotes a complex conjugate. A spatial Fourier transformation of the cross-spectral matrix/tensor in the homogeneous θ-direction provides an azimuthal mode number, m, dependent cross-spectral matrix given by:

$$\Phi_{\alpha\beta}(r, r', f, m) = \int S_{\alpha\beta}(r, r', f, \Delta\theta)\mathrm{e}^{\mathrm{i}m\Delta\theta}\,\mathrm{d}(\Delta\theta). \tag{3.3}$$

As shown in Lumley (1970), the spectral correlation tensor $\Phi_{\alpha\beta}(r, r'; f, m)$ is a kernel in the integral equation to find the POD modes for different frequencies f, and azimuthal mode numbers, m,

$$\int \Phi_{\alpha\beta}(r, r'; m, f)\varphi^{(n)}_\beta(r'; m, f)r'\,\mathrm{d}r' = \lambda^{(n)}(m, f)\varphi^{(n)}_\alpha(r; m, f). \tag{3.4}$$

Here superscript n denotes POD mode number. The solution of (3.4) gives a complete set of orthonormal eigenfunctions $\varphi^{(n)}_\alpha(r; m, f)$ with corresponding positive eigenspectra $\lambda^{(n)}(m, f)$. Any local velocity realization can be represented as a sum of the eigenfunctions,

$$u_\alpha(r, \theta, t) = \sum_{n=1}^{\infty}\sum_{m=0}^{\infty}\int a^{(n)}(m, f)\varphi^{(n)}_\alpha(r; m, f)\exp(2\pi\mathrm{i} f t)\exp(\mathrm{i}m\theta)\,\mathrm{d}f. \tag{3.5}$$

In (3.5) the coefficients $a^{(n)}(m, f)$ are obtained by projection of the eigenmodes onto individual realizations of the flow field. The spectral correlation tensor $\Phi_{\alpha\beta}(r, r'; m, f)$ can be expanded as

$$\Phi_{\alpha\beta}(r, r'; m, f) = \sum_{n=1}^{\infty} \lambda^{(n)}(m, f)\varphi_{\alpha}^{(n)}(r; m, f)\left\{\varphi_{\beta}^{(n)}(r'; m, f)\right\}^{*}. \tag{3.6}$$

The eigenspectra $\lambda^{(n)}(m, f)$ represent the energy distribution in frequency–azimuthal mode number space for each of the extracted POD modes. From the above discussion, it is apparent that the problem of finding the POD modes is reduced to solving a number of integral equations (3.4) with m and f as parameters.

In order to extract the POD modes, all components of the $\Phi_{\alpha\beta}$-matrix must be obtained. Unfortunately, the term Φ_{wv} cannot be measured directly using the X-wire rakes. However, it can be obtained from mass conservation requirements using a procedure originally described in Ukeiley & Glauser (1995) and Ukeiley *et al.* (2001). A Fourier transform of the mass conservation equation gives

$$\frac{\partial \hat{u}(r, \theta, f)}{\partial x} + \frac{1}{r}\frac{\partial(r\hat{v}(r, \theta, f))}{\partial r} + \frac{1}{r}\frac{\partial \hat{w}(r, \theta, f)}{\partial \theta} = 0. \tag{3.7}$$

In order to estimate the streamwise derivative, a Taylor's frozen field approximation is used. This assumes a constant convective speed of the flow structure at a given cross-section in the jet. Numerous experiments (e.g. Bradshaw *et al.*; 1964, Davies, Ko & Bose 1967; Arndt *et al.* 1997) have indicated that the large-scale jet structure convects at approximately 60 % of the local jet centreline mean velocity ($U_c \approx 0.6U_{max}$). After applying the constant convective speed hypothesis in the x-direction one obtains

$$\frac{\partial}{\partial x} = -\frac{1}{U_c}\frac{\partial}{\partial t} = -2\pi \mathrm{i} f \frac{1}{U_c} = \mathrm{i}k_x \tag{3.8}$$

The complex conjugate of (3.7) is and is subsequently multiplied by $\hat{v}(r', \theta', f)$ and an average is taken over multiple ensembles. After performing a spatial Fourier transform in the θ-direction, equation (3.7) can be rewritten in terms of $\Phi_{\alpha v}$ as

$$\mathrm{i}k_x\Phi_{uv} + \frac{1}{r}\frac{\partial(r\Phi_{vv})}{\partial r} + \mathrm{i}\frac{m}{r}\Phi_{wv} = 0. \tag{3.9}$$

From the above relation, Φ_{wv} can be easily calculated. The remaining terms Φ_{vu}, Φ_{wu} and Φ_{vw} can be found using the property that the Φ-matrix is Hermitian,

$$\Phi_{\alpha\beta}(r, r'; m, f) = \Phi_{\beta\alpha}^{*}(r', r; m, f). \tag{3.10}$$

All the required $\boldsymbol{S}$-matrix measurements are performed over half of the (r, θ)-plane, i.e. for $\Delta\theta = 0 \ldots \pi$ with values for $\Delta\theta = 0 \ldots 2\pi$ obtained by exploiting the symmetry property in the θ-direction, $\theta \to -\theta$, $u \to u$, $v \to v$, $w \to -w$, which gives the following symmetry relations for the S-matrix components

$$S_{\alpha\beta}(r, r', 2\pi - \Delta\theta, f) = \begin{cases} -S_{\alpha\beta}(r, r', \Delta\theta, f), & \alpha = w, \text{ or } \beta = w \\ +S_{\alpha\beta}(r, r', \Delta\theta, f), & \text{otherwise.} \end{cases}$$

3.2. *Numerical implementation*

Since the acquired velocity time-series are discrete in both time and space, careful consideration must be given to the minimization of temporal and spatial aliasing and this is described in some detail in the Appendix. There it is shown that a 10 kHz Nyquist frequency (i.e. 20 kHz sample frequency) combined with the use of anti-alias

filters both prevented temporal aliasing and provided more than sufficient bandwidth for the cross-spectral measurements.

The experiments were first performed with $\Delta\theta = 15^\circ$ which allows resolution of azimuthal mode numbers $m = 0 \ldots 11$. In order to assess the degree of spatial aliasing of azimuthal modes, the experiments were subsequently repeated at selected streamwise locations with $\Delta\theta = 7.5^\circ$ corresponding to resolved azimuthal mode numbers $m = 0 \ldots 23$. Comparison of the POD results showed that only comparatively low-energy azimuthal modes $m \geqslant 7$ exhibited aliasing. More importantly, *the most energetic azimuthal mode numbers which form a focus of this study are virtually identical*. In this paper results from both experiments are compared at representative locations.

In order to ensure stationary cross-spectral statistics, convergence tests were performed. For all radial and streamwise locations, sampling fluctuating velocity in blocks $N_p = 1024$ points for a total of $N_b = 400$ blocks yielded fully converged cross-spectral statistics.

A fast Fourier transform (Bendat & Piersol 1986) of the discrete velocity fluctuation time-series (with a Hanning window to suppress side-lobe spectral leakage) is used to compute the Fourier transform of the velocity components and thus obtain the $S_{\alpha\beta}(r, r', \Delta\theta, f)$-matrix (3.2). A discrete Fourier transform of the $\boldsymbol{S}$-matrix in the azimuthal θ-direction is used to calculate the $\Phi_{\alpha\beta}(r, r', f, m)$-matrix.

3.2.1. *Calculation of the POD eigenmodes*

At a fixed x/D location $\Phi_{\alpha\beta}$ is known at a finite number of positions across the jet $\{r_i, \theta_j\}$, $i = 1, \ldots, N_r$, $j = 1 \ldots N_\theta$ where $N_r = 7$ is the number of X-wire probes in one rake and $N_\theta = 2\pi/\Delta\theta = 24$ or 48 (depending on the probe rake utilized) is the number of azimuthal measurement locations. Consequently, the integral from eq. (3.4) should be replaced with a finite quadrature form. The finite approximation of the integral equation (3.4) for $3k$-vector $\boldsymbol{\varphi} = (\varphi_u, \varphi_v, \varphi_w)^T$, $\boldsymbol{\varphi}_\alpha = \{\varphi_\alpha(r_i; f, m)\}_{i=1}^{k}$ can be written in the following form:

$$\sum_{j=1}^{k} \Phi_{\alpha\beta}(r_i, r_j; f, m) w(r_j) \varphi_\beta^{(n)}(r_j; f, m) \frac{r_j + r_{j+1}}{2} \Delta r = \lambda^{(n)}(f, m) \varphi_\alpha^{(n)}(r_i; f, m), \tag{3.11}$$

or

$$\Phi_{\alpha\beta} \boldsymbol{W} \boldsymbol{\varphi}_\beta = \frac{\lambda}{\Delta r} \boldsymbol{\varphi}_\alpha, \tag{3.12}$$

where the summation is applied on repeated indices and the $\boldsymbol{W}$-matrix is a weighting $[k \times k]$ matrix, $\boldsymbol{W} = [\overbrace{\boldsymbol{w}, \ldots, \boldsymbol{w}}^{k\text{-columns}}]$, where $\boldsymbol{w}$ is a weighting k-vector

$$\boldsymbol{w} = 0.5\tilde{r}(1), \overbrace{1 \cdot \tilde{r}(2), 1 \cdot \tilde{r}(3), \ldots, 1 \cdot \tilde{r}(N_r - 1)}^{k-2}, 0.5\tilde{r}(N_r)\}^T \tag{3.13}$$

where $\tilde{r}(j) = 0.5(r_j + r_{j+1})$, $\Phi_{\alpha\beta} = \{\Phi_{\alpha\beta}(r_i, r_j; f, m)\}_{i,j=1}^{k,k}$ is the $[k \times k]$ Hermitian matrix and $\Delta r = 6.35\,\text{mm}$ is the spacing between probes in the rake. After multiplication, the $\Phi\boldsymbol{W}$-matrix is no longer Hermitian. We next multiply (3.11) by $\boldsymbol{W}^{1/2}$ (see Glauser *et al.* 1987) from the left and rearrange to obtain

$$\boldsymbol{W}^{1/2} \Phi_{\alpha\beta} \boldsymbol{W} \varphi_\beta = \left(\boldsymbol{W}^{1/2} \Phi_{\alpha\beta} \boldsymbol{W}^{1/2}\right) \left(\boldsymbol{W}^{1/2} \boldsymbol{\varphi}_\beta\right) = \frac{\lambda}{\Delta r} \left(\boldsymbol{W}^{1/2} \boldsymbol{\varphi}_\alpha\right) \tag{3.14}$$

or

$$\widetilde{\Phi}_{\alpha\beta}\,\widetilde{\varphi}_{\beta} = \frac{\lambda}{\Delta r}\widetilde{\varphi}_{\alpha}. \tag{3.15}$$

Now $\widetilde{\Phi}_{\alpha\beta} = \boldsymbol{W}^{1/2}\Phi_{\alpha\beta}\boldsymbol{W}^{1/2}$ is a Hermitian matrix with $\lambda/\Delta r$ and $\widetilde{\boldsymbol{\varphi}}_{\alpha} = \boldsymbol{W}^{1/2}\boldsymbol{\varphi}_{\alpha}$ the corresponding eigenvalues and eigenvectors, respectively. The matrix equation (3.14) was solved using a Hermitian matrix solver in Matlab. After a back transformation $\boldsymbol{\varphi}_{\alpha} = \boldsymbol{W}^{-1/2}\widetilde{\boldsymbol{\varphi}}_{\alpha}$, a finite set of k orthogonal spatial modes at the discrete spatial points $\varphi_{\alpha}^{(n)}(r_i; f, m)$ with corresponding eigenspectra $\lambda^{(n)}(f, m)$ are obtained.

4. Experimental results

In this section experimental results from the implementation of the POD in the axisymmetric jet are presented. These results are divided into two major categories. In the first part, the POD eigenmodes and associated eigenspectra are obtained for streamwise locations ranging from $x/D = 3$ to 12. These POD modes provide a structural template for the local, time-mean jet coherent structure in a mixed physical–Fourier domain. In the second part, the POD modes are projected onto instantaneous cross-stream flow field realizations obtained via linear stochastic estimation (LSE), and aspects of the local jet coherent structure dynamics are recovered.

4.1. *POD modal energy distribution*

Consideration is first given to the rate of energy convergence of the POD modes with mode number n as expressed through their respective eigenspectra, $\lambda^{(n)}(f, m)$. As noted earlier, the eigenspectra provide the modal energy distribution in temporal frequency f, and azimuthal mode number m, space. Therefore, the kinetic energy in each POD mode is obtained by summing over all frequencies and azimuthal mode numbers, $\sum_{f,m}\lambda^{(n)}(f, m)$. The energy content in each individual POD mode, $E_r(n)$, relative to the total resolved energy is then given by

$$E_r(n) \equiv \frac{\sum\limits_{f,m}\lambda^{(n)}(f, m)}{\sum\limits_{n}\sum\limits_{f,m}\lambda^{(n)}(f, m)}. \tag{4.1}$$

The cumulative energy, $E_c(n)$, provides a direct measure of the rate of energy convergence of the POD modes with n and is given by

$$E_c(n) \equiv \frac{\sum\limits_{k=1}^{n}\sum\limits_{f,m}\lambda^{(k)}(f, m)}{\sum\limits_{n}\sum\limits_{f,m}\lambda^{(n)}(f, m)}. \tag{4.2}$$

Figure 11 presents both the relative energy content E_r and the cumulative energy E_c of the POD modes at four representative streamwise locations in the jet. At $x/D = 3$ the first POD mode accounts for approximately 41 % of the total kinetic energy and this value increases with streamwise distance to 48 % at $x/D = 12$. Examination of E_c indicates that the first four POD modes account for 84 % of the total kinetic energy at $x/D = 3$ and 87 % at $x/D = 12$. Hence, it is apparent that the rate of energy convergence with POD mode number is not a strong function of streamwise location. The rapid energy convergence with mode number at each streamwise location bodes well for the possibility of developing a low-dimensional description of the turbulent axisymmetric jet flow field (e.g. Aubry *et al.* 1988; Ukeiley & Glauser 1995; Taylor, Ukeiley & Glouser 2001).

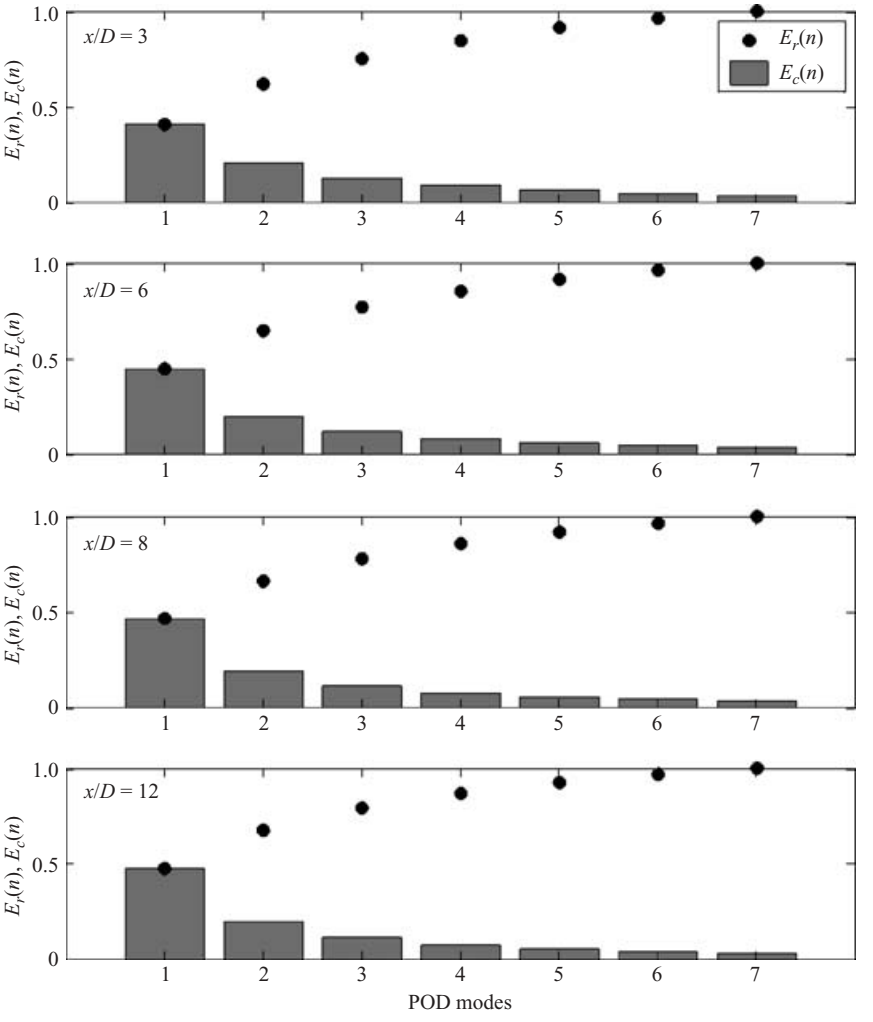

FIGURE 11. Relative and cumulative energy content of the POD modes at representative x/D locations.

4.2. *POD eigenspectra*

Figure 12 presents the streamwise evolution of POD mode $n=1$ eigenvalue spectra, $\lambda^{(1)}(f,m)$. In this figure, the frequency is expressed as a Strouhal number based on nozzle diameter, D, and jet exit velocity, U_j. Note that these POD eigenvalue spectra are derived from the full $\Phi_{\alpha\beta}$ matrix. The POD mode-1 energy content clearly grows with streamwise distance (note the different ordinate scales used in figure 12). At $x/D=3$, energy is distributed over a wide range of azimuthal mode numbers but there is a clear tendency for lower azimuthal mode numbers to dominate with increasing downstream distance. By $x/D=10$, figure 12 shows that the peaks at azimuthal mode numbers $m=1$ and $m=2$ dominate the spectrum. The eigenvalue spectra also indicate that a dominant portion of the fluctuation energy occurs for $St_D<0.5$.

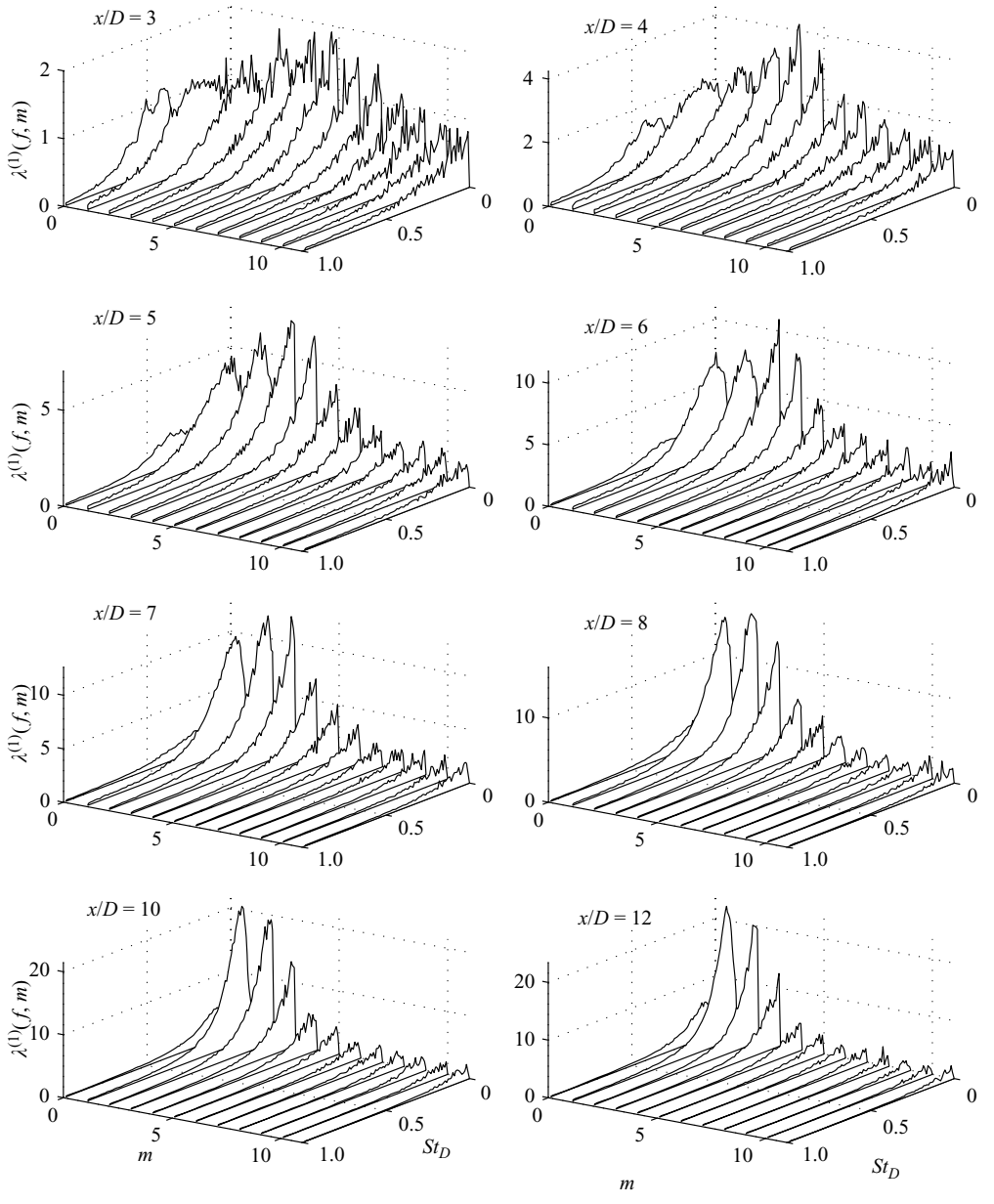

FIGURE 12. Eigenspectra for the first POD mode in the (St_D, m) domain.

Figure 13 presents the streamwise evolution of the POD mode $n = 2$ eigenvalue spectra, $\lambda^{(2)}(f, m)$. This figure indicates that the mode-2 eigenvalue spectra are dominated by a peak at azimuthal mode $m = 1$ at each streamwise location. As was the case for mode $n = 1$, this peak grows in prominence relative to the other azimuthal modes with streamwise distance.

The eigenvalue spectra of figures 12 and 13 may be integrated with respect to frequency (or equivalently, St_D) in order to more clearly indicate the streamwise variation in azimuthal-mode energy content of the jet coherent structure. The relative

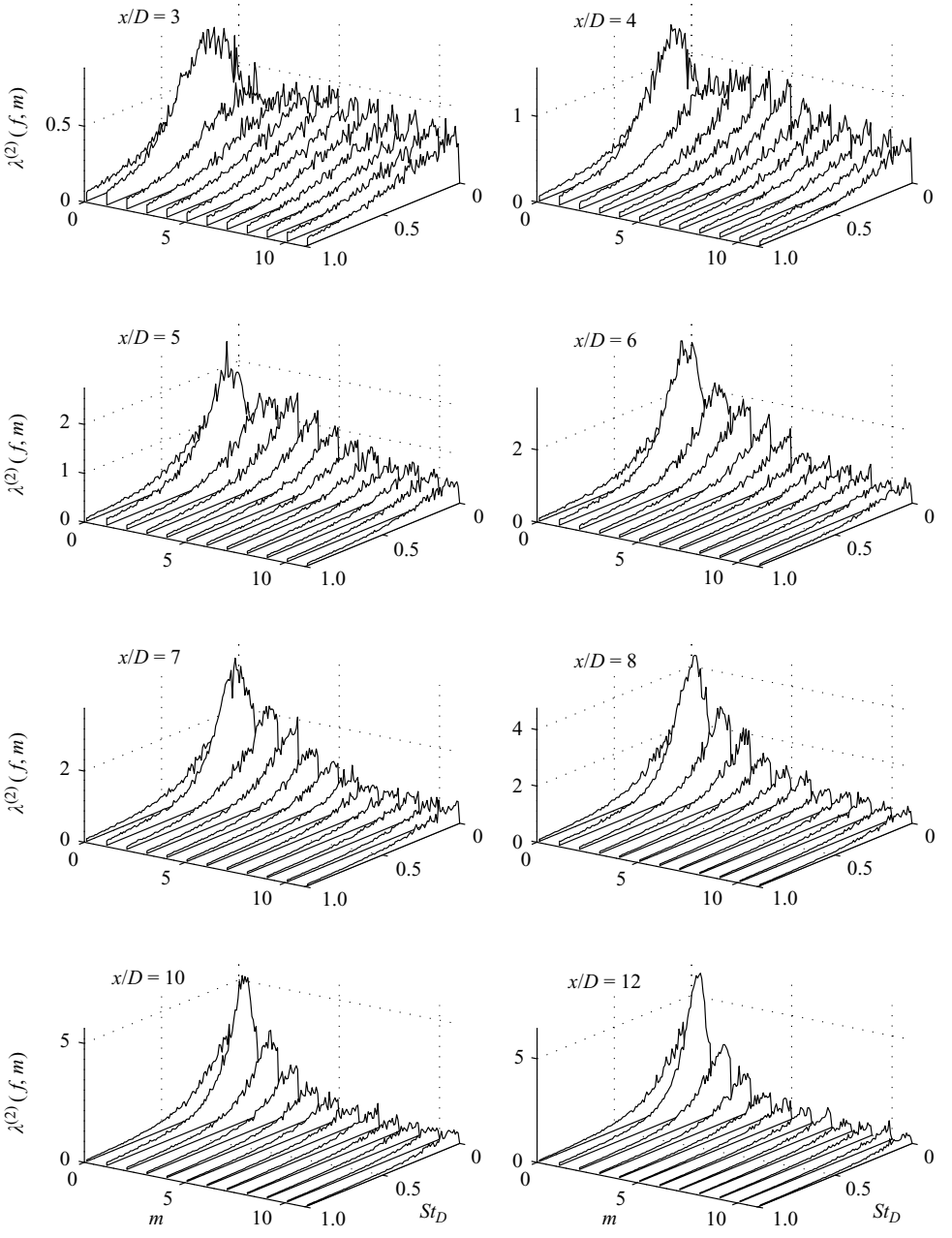

FIGURE 13. Eigenspectra for the second POD mode in the (St_D, m) domain.

azimuthal energy distribution, $\xi^{(n)}(m)$, is defined as

$$\xi^{(n)}(m) \equiv \frac{\sum_f \lambda^{(n)}(f, m)}{\sum_n \sum_m \sum_f \lambda^{(n)}(f, m)}. \tag{4.3}$$

Figure 14 presents the streamwise variation of the azimuthal energy distribution $\xi^{(n)}(m)$ for POD modes $n = 1$ and $n = 2$. This figure shows an initially broad

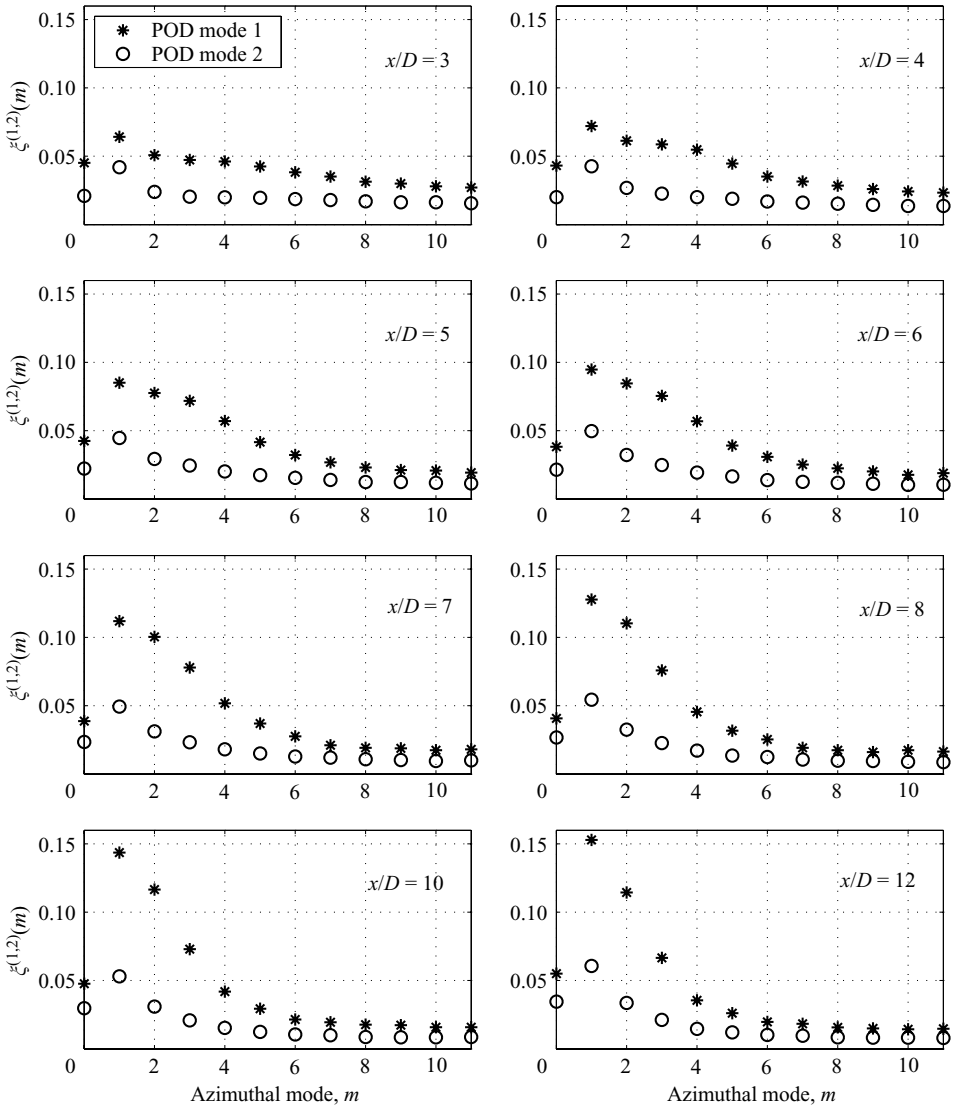

FIGURE 14. Azimuthal mode energy distribution $\xi^{(n)}(m)$ for POD modes $n=1$ and $n=2$.

distribution of energy over multiple azimuthal modes. The figure also clearly shows the preferred growth of lower, non-zero azimuthal mode numbers with increasing streamwise distance. However, the azimuthal mode $m=1$ is observed to dominate both POD modes at all streamwise locations $3 \leqslant x/D \leqslant 12$ and this relative dominance clearly grows with streamwise distance. In contrast, the axisymmetric mode $m=0$ appears neutral, exhibiting negligible streamwise growth or decay

The results shown in figure 14 were obtained from the rake with $\Delta\theta = 15^{\circ}$. In order to assess the degree of spatial aliasing of azimuthal modes, the experiment was repeated with $\Delta\theta = 7.5^{\circ}$. Figure 15 compares $\xi^{(n)}(m)$ for POD modes 1 and 2 as obtained from both experiments. Results are compared at two representative streamwise locations, $x/D = 3$ and 6. The comparison shown in figure 15 may be

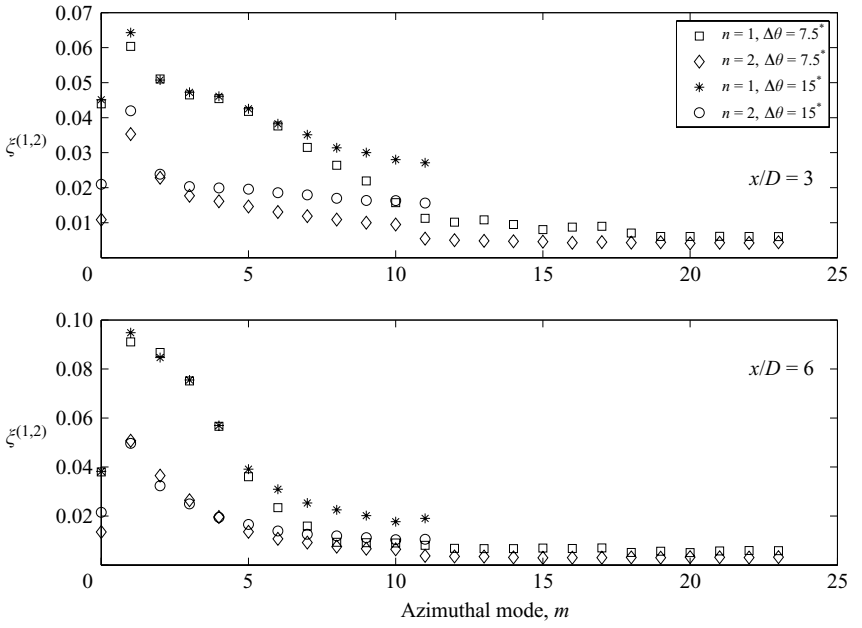

FIGURE 15. Azimuthal mode energy distribution $\xi^{(n)}(m)$ for POD modes $n = 1$ and $n = 2$.

considered representative of other streamwise locations. This figure clearly shows that only comparatively low-energy azimuthal modes $m \geqslant 7$ are significantly aliased. In fact, the lower, more energetic azimuthal mode distribution of energy is nearly identical for the two experiments. The aliasing of high azimuthal mode numbers is observed to be more significant for the $x/D = 3$ location as one would expect. Figure 15 shows unequivocally that spatial aliasing is not a significant factor in the streamwise evolution of $\xi^{(n)}(m)$ shown in figure 14. In particular, the dominance of azimuthal mode $m = 1$ is not due to azimuthal aliasing.

As noted previously, Citriniti & George (2000) and Jung *et al.* (2004) utilized the POD to examine the large-scale structure in the axisymmetric turbulent jet. Both implementations involved measurement of POD eigenspectra based on only the streamwise fluctuating component. The eigenspectra presented in figures 12 and 13 result from an implementation of the POD derived from the measurement of the full $\Phi_{\alpha\beta}$ matrix and, consequently, contain the contribution from all three fluctuating velocity components. In order to form a basis for comparison with previous studies, eigenfunctions and corresponding eigenspectra based on only the streamwise fluctuating component can be obtained from the diagonal element Φ_{uu} by means of a scalar implementation of the POD,

$$\int \Phi_{uu}(r, r'; m, f)\varphi_u^{(n)}(r'; m, f)r' \, \mathrm{d}r' = \lambda_u^{(n)}(m, f)\varphi_u^{(n)}(r; m, f), \tag{4.4}$$

where $\varphi_u^{(n)}(r; m, f)$ and $\lambda_u^{(n)}(m, f)$ are the u-component eigenfunction and associated eigenvalue spectrum, respectively. Similarly, eigenfunctions and corresponding eigenspectra based on the v and w fluctuating velocity components can be obtained from equation (4.4) with Φ_{vv} and Φ_{ww} the respective kernels.

For POD modes $n = 1$ and $n = 2$, eigenspectra $\lambda_u^{(n)}(m, f)$ based on the streamwise component were obtained and subsequently integrated over all frequencies to obtain

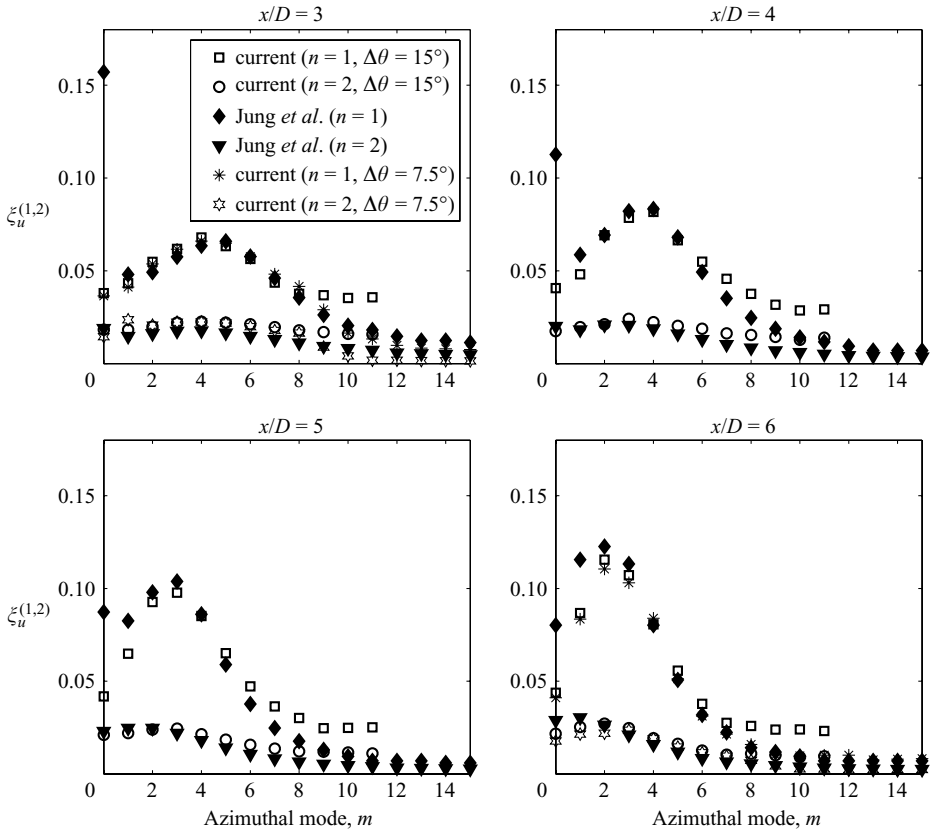

FIGURE 16. Comparison of the azimuthal mode number dependence of u-component eigenspectra with values from Jung *et al.* (2004).

$\xi_u^{(n)}(m)$, which is defined as

$$\xi_u^{(n)}(m) \equiv \frac{\sum_f \lambda_u^{(n)}(f,m)df}{\sum_n \sum_m \sum_f \lambda_u^{(n)}(f,m)df}. \tag{4.5}$$

The numerator is the integral of the u-component eigenvalue spectrum over all frequencies and the denominator is the total resolved u-component energy. Figure 16 makes a direct comparison of the azimuthal distribution of energy $\xi_u^{(n)}(m)$ as determined in this study with corresponding values obtained by Jung *et al.* (2004). The comparison is made at several streamwise locations in the near field of the jet. The results of Jung *et al.* (2004) were obtained in an axisymmetric jet at $Re_D = 156\,800$ as compared to $Re_D = 380\,800$ in the current study. The important point to note is that, despite the disparity in Reynolds number, the agreement in modal distribution of energy is quite remarkable. Both show a shift of peak energy from $m = 4, 5$ near $x/D = 3$ to lower azimuthal mode numbers with increasing streamwise distance, and this leads to $m = 2$ dominating beyond the tip of the jet core ($x/D = 6$). The favourable agreement in the azimuthal distribution of energy $\xi_u^{(n)}(m)$ shown in figure 16 is consistent with the assertion of Glauser (1987) that once Re_D is sufficiently high then there is little dependence of the modal energy distribution on Reynolds number.

Figure 16 shows that disparities do occur for the highest mode numbers ($m \geqslant 7$) and this is clearly a manifestation of the spatial aliasing of higher wavenumber modes in the current study as established previously in figure 15. Note that for the cases $x/D = 3$ and 6 shown in figure 16, results from the current study with $\Delta\theta = 7.5^\circ$ are included and agree with those of Jung *et al.* (2004) even at the highest azimuthal mode numbers. The probe array used by Jung *et al.* (2004) resolves $m \leqslant 15$.

As shown in figure 16, the largest disparity between the current measurements and those of Jung *et al.* (2004) occurs for the axisymmetric mode, $m = 0$. Its modal energy content is initially quite high in relation to the helical modes in the experiments of Jung *et al.* (2004) but decays rapidly with streamwise distance. In the current experiment, the $m = 0$ mode is at a low level and is essentially neutral, exhibiting virtually no growth with x/D. This disparity in behaviour is probably associated with differences in initial conditions between the jet flow field facilities. Indeed, disparities in the $m = 0$ mode are also noted in comparing the results of Jung *et al.* (2004) with those of Tinney, Glauser & Ukeiley (2005). It is well known that azimuthally coherent acoustic forcing in any free shear flow facility will influence the initial evolution of the flow as described in numerous references (e.g. Gutmark & Ho 1983 and Thomas 1991). Since there is a large disparity between acoustic wavelengths and the wavelength of the initial shear layer vortical instability, their coupling can occur only at the receptivity site at the nozzle lip as described by Tam (1986). The nozzle diameter is invariably small in relation to background acoustic disturbances so that the forcing of the nascent shear layer is azimuthally coherent and will excite the axisymmetric mode that is the most unstable mode at the nozzle lip (Cohen & Wygnanski 1987). In the current study, extraordinary precautions were taken to avoid facility-dependent acoustic forcing of the nascent jet shear layer (which would be axisymmetric). This does not appear to be the case in the study by Jung *et al.* (2004). Consequently, it is not surprising to observe disparities in the $m = 0$ mode energy content. The key point to note, however, is that $m = 0$ is in decay in the measurements of Jung *et al.* (2004) and tends towards values similar to those observed in the current experiment.

In order to provide a measure of the relative energy content contributed by each fluctuating velocity component towards the total kinetic energy of the jet coherent structure, the ratio $\zeta_r(n;\alpha)$ is defined as,

$$\zeta_r(n;\alpha) \equiv \frac{\sum\limits_{f,m} \lambda_\alpha^{(n)}(f,m)}{\sum\limits_{n}\sum\limits_{\alpha}\sum\limits_{f,m} \lambda_\alpha^{(n)}(f,m)}, \tag{4.6}$$

where α represents any fluctuating velocity component (u, v, or w). The numerator is the total modal energy content for a given fluctuating velocity component. This is normalized by the total energy contained in the u-, v-, and w- component eigenvalues as obtained from respective scalar implementations of the POD. Hence, the denominator is a metric that is at least related (but not necessarily equal) to the total energy of the jet large-scale structure. Figure 17 presents the relative energy $\zeta_r(n;\alpha)$ for each velocity component versus POD mode number as obtained at two representative streamwise locations in the jet. The behaviour of $\zeta_r(n;\alpha)$ is not a strong function of streamwise location and the results presented for $x/D = 3$ and 8 may be considered representative. Note that the energy content in the streamwise component is dominant, followed, in turn, by the azimuthal and radial components. For POD mode 1 the azimuthal energy content is 53–59 % of that in the streamwise component while the radial component accounts for 30–36 %. As shown in figure 17, similar

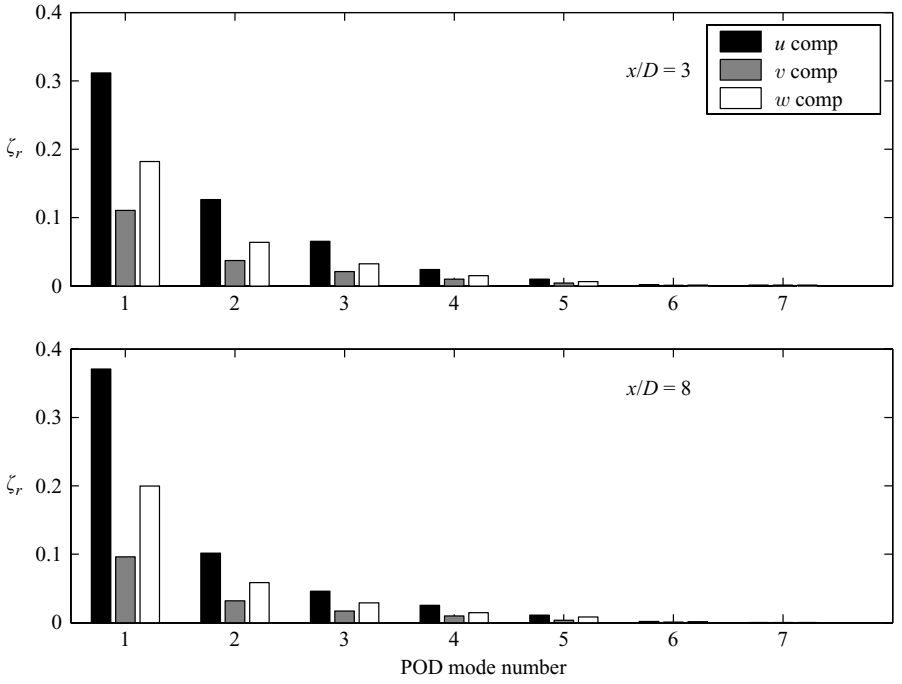

FIGURE 17. Relative energy in streamwise, radial and azimuthal components of the POD modes.

values are also observed for higher POD mode numbers. It is apparent that the sum of the modal energy contained in the azimuthal and radial fluctuating components is comparable with that in the streamwise component. Since the azimuthal and radial components contain significant modal energy relative to the streamwise component, there is a possibility of losing flow physics by neglecting the v and w-components and this provides one motivation for the vector implementation of the POD presented in this paper. Finally, the rapid energy convergence with mode number is noted, which is consistent with the results presented previously in figure 11.

Eigenspectra based on the w fluctuating velocity component were obtained from equation (4.4) with Φ_{ww} the kernel. The eigenspectra $\lambda_w^{(n)}(m, f)$ were subsequently integrated over all frequencies to obtain $\xi_w^{(n)}(m)$. Figure 18 presents $\xi_w^{(n)}(m)$ for POD modes $n = 1$ and $n = 2$, at representative streamwise locations in the near field of the jet. The streamwise variation in the azimuthal distribution of energy for the w-component is distinctly different from that previously presented for the u-component. In particular, azimuthal mode $m = 1$ is observed to be dominant at each streamwise location. At $x/D = 6$, for example, figure 16 shows the dominance of azimuthal mode $m = 2$ for the u-component while figure 18 shows the dominance of $m = 1$ for the w-component. Note that in figure 18 results from experiments with both $\Delta\theta = 15^\circ$ and $\theta = 7.5^\circ$ are included for $x/D = 3$ and 6. Note again that the variation of $\xi_w^{(n)}(m)$ is virtually identical for the dominant mode numbers indicating that they are not influenced by spatial aliasing.

In a similar manner, figure 19 presents $\xi_v^{(n)}(m)$ at representative x/D locations in the jet near field as derived from eigenspectra $\lambda_v^{(n)}(m, f)$. This figure shows that the v-component is initially dominated by the axisymmetric mode $m = 0$. Only with increased x/D does the $m = 1$ mode gradually become comparable to the $m = 0$ mode.

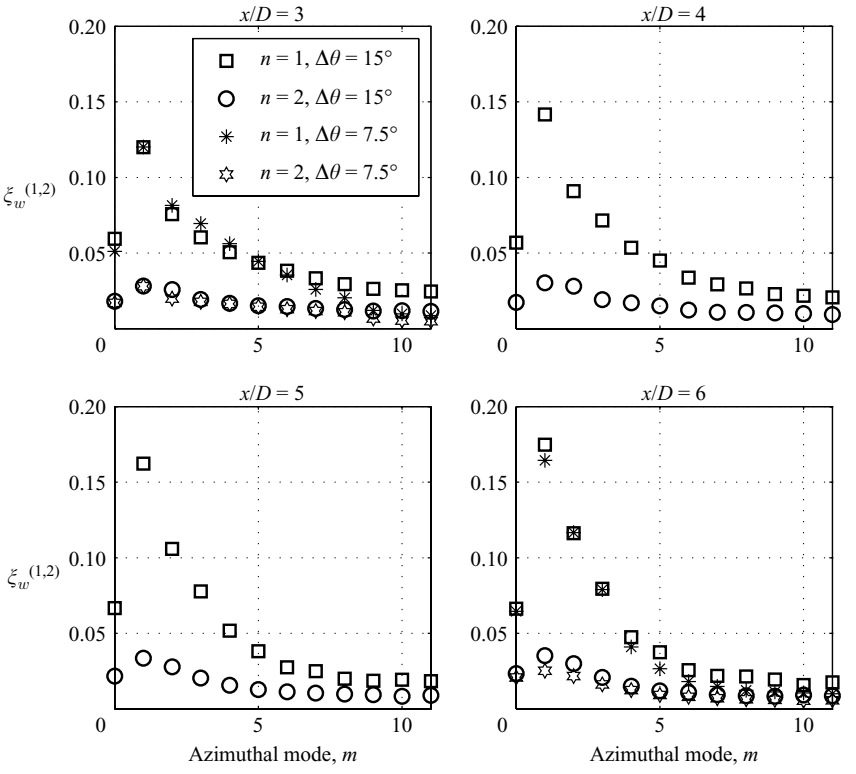

FIGURE 18. Comparison of the azimuthal mode number dependence of w-component eigenspectra.

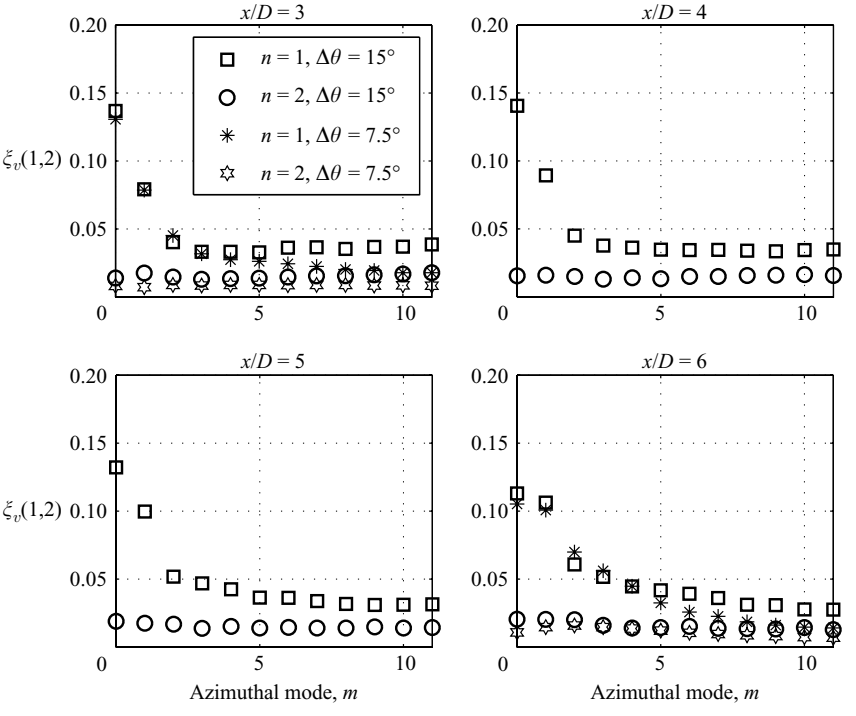

FIGURE 19. Comparison of the azimuthal mode number dependence of v-component eigenspectra.

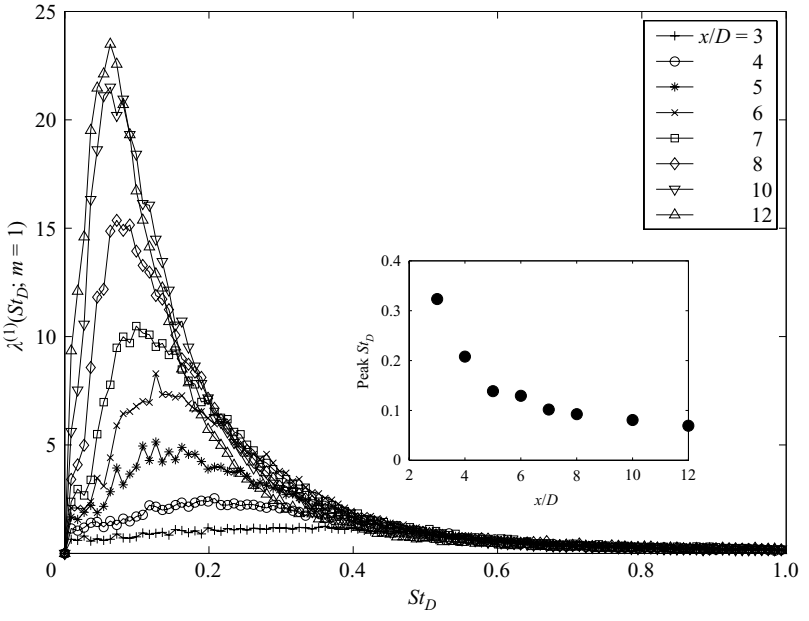

FIGURE 20. POD mode-1 eigenspectra for azimuthal mode number $m = 1$.

4.3. *Strouhal number dependence of the POD eigenspectra*

Figure 20 presents POD mode $n = 1$ eigenspectra for azimuthal mode $m = 1$ as obtained at several streamwise locations throughout the near field of the jet. The abscissa is Strouhal number, St_D (based on the jet exit velocity, U_j, and the nozzle diameter, D). The eigenspectra of figure 20 each feature a broad peak and the St_D associated with this peak decreases with x/D in a continuous manner as shown in the inset diagram of the figure.

The local temporal frequency associated with a particular convected POD mode is proportional to the convective speed of the structure past the fixed measurement location and inversely proportional to a local characteristic length scale associated with the structure. The convective speed will be some fraction of the local jet centreline velocity, U_{max}. Upstream of the jet potential core, it is reasonable to expect the relevant local length scale to be related to a characteristic axisymmetric shear-layer length scale like the *local* momentum thickness, θ. Figure 21(a) presents the same eigenspectra as shown in figure 20 but with the frequency scaled in terms of Strouhal number $St_\theta = f\theta/U_{max}$. In order to properly emphasize the spectral peak, the eigenspectra are equivalently presented by plotting the product $St_\theta * \lambda^{(1)}(St_\theta; m = 1)$ versus St_θ on a logarithmic abscissa. This figure clearly shows that the peaks in the eigenvalue spectra occur at a constant value of $St_\theta \approx 0.035$. This scaling of the eigenspectra peak with St_θ is consistent with the notion that the large-scale structure represented by the POD is a manifestation of modes of instability of the axisymmetric jet shear layer.

Figure 21(b) presents similar results for the POD mode $n = 2$, $m = 1$ eigenspectra where $St_\theta * \lambda^{(2)}(St_\theta; m = 1)$ is also presented as a function of $\log(St_\theta)$. Again, for locations upstream and near the tip of the jet core, the eigenspectra peaks occur at a constant $St_\theta \approx 0.036$ which is nearly the same value as noted for $\lambda^{(1)}(St_\theta; m = 1)$. Note that the scaling of the spectral peak with St_θ breaks down beyond the jet potential core as would be expected.

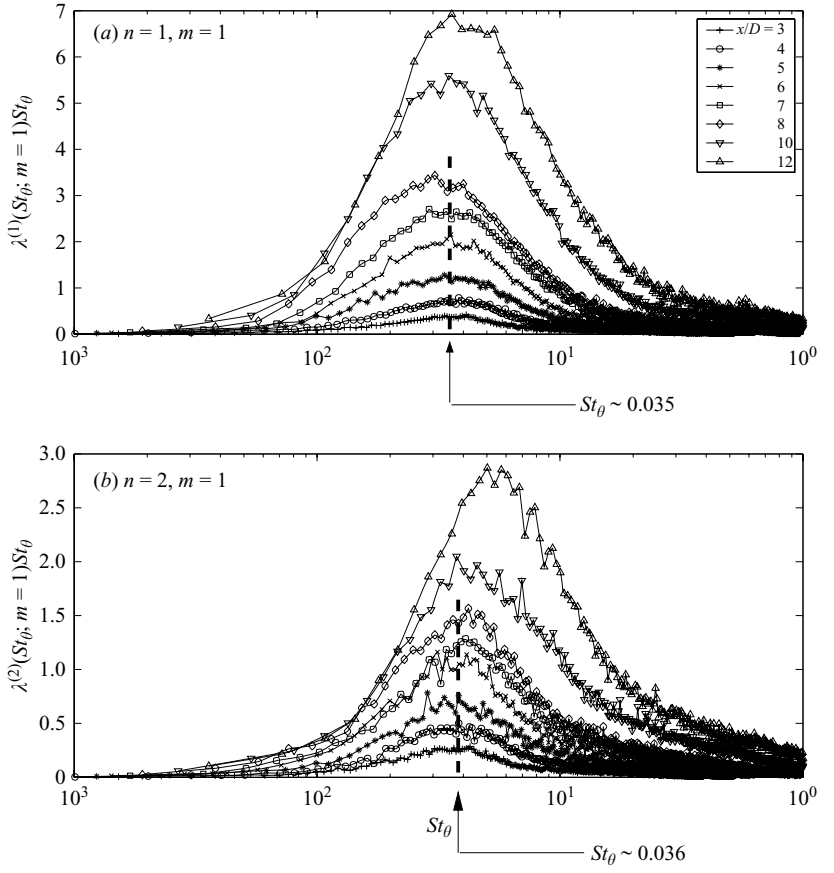

FIGURE 21. POD mode-1 and -2 eigenspectra for azimuthal mode number $m = 1$.

The scaling of the peaks in the eigenspectra with St_θ is not restricted to the azimuthal mode $m = 1$. For example, figure 22 presents similarly scaled eigenspectra, $\lambda^{(1)}(St_\theta; m = 2)$. As before, for x/D locations upstream and near the tip of the jet core, there is a well-defined spectral peak which occurs at constant St_θ; in this case $St_\theta \approx 0.025$. This figure serves to illustrate the general finding that higher azimuthal mode numbers are associated with lower St_θ values at peak amplitude. For example, although not shown, it was found that the peak in the eigenspectra $\lambda^{(1)}(St_\theta; m = 0)$ occurred at a constant $St_\theta \approx 0.048$.

Figure 22 also illustrates the breakdown in the scaling of the spectral peak with constant St_θ that occurs beyond the tip of the jet core.

The St_D values associated with local maxima in $\lambda^{(1)}(St_D, m = 1)$ (as shown in the inset of figure 20) are considerably lower than the measured jet column mode shown in the autospectra of figure 7. Indeed, peaks associated with $\lambda^{(1)}(St_D, m = 2)$ occur at even lower St_D values. At first sight this seems puzzling since the centreline spectra show maximum energy near $St_D = 0.4$ and yet the most energetic helical POD modes are associated with lower St_D. Resolution of this issue comes from examination of the eigenspectra associated with the axisymmetric mode, $\lambda^{(n)}(St_D, m = 0)$. These are found to exhibit spectral peaks in the vicinity of the tip of the jet core at $St_D \approx 0.44$, thereby matching the jet column mode. In this sense, the jet column mode of instability is actually a superposition of POD modes with $m = 0$.

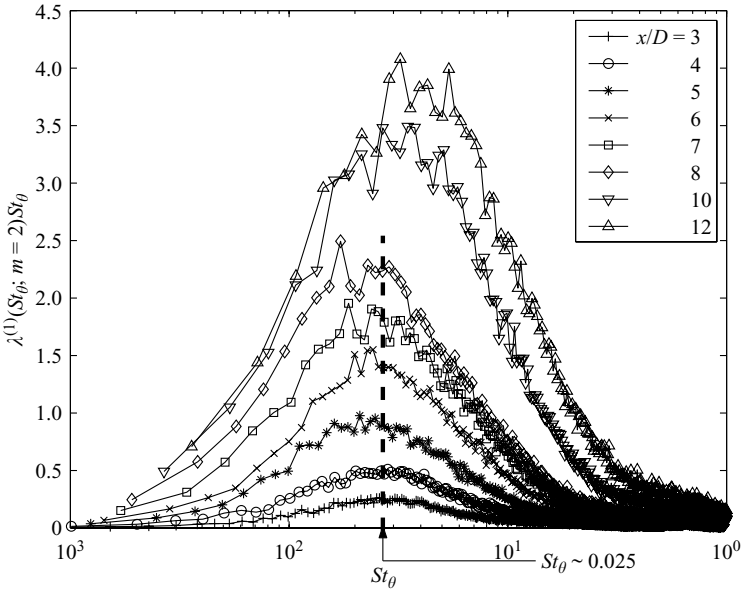

FIGURE 22. POD mode-1 eigenspectra for azimuthal mode number $m = 2$.

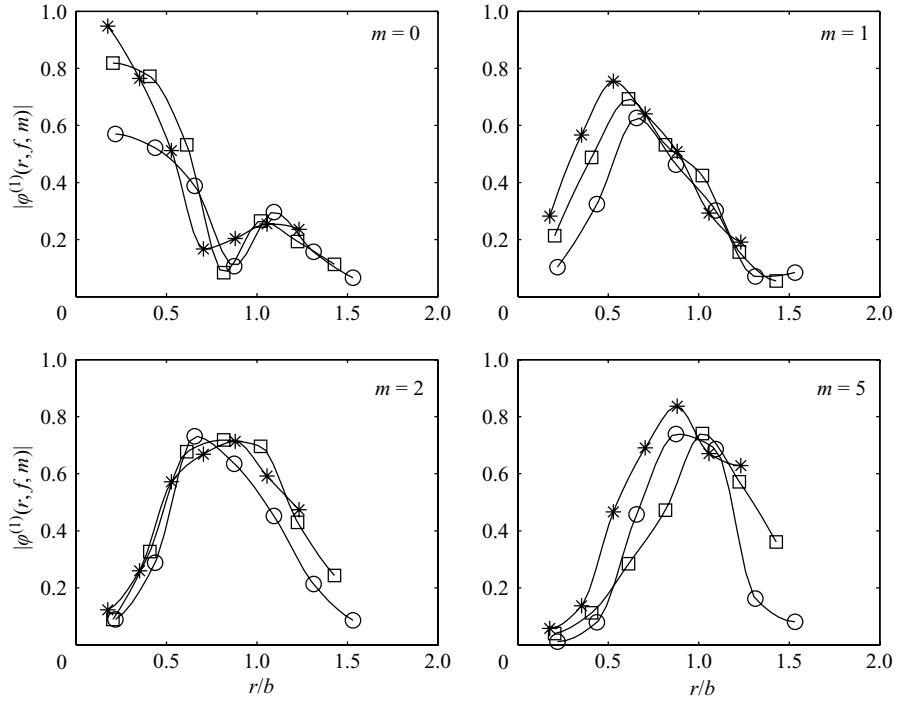

FIGURE 23. POD mode-1 eigenfunction modulus for indicated azimuthal mode numbers and x/D locations: ○, $x/D = 4$; □, represent $x/D = 6$; ∗, $x/D = 8$.

4.4. *POD eigenmode shape*

Figure 23 presents the modulus of the POD mode-1 eigenfunction, $|\varphi^{(1)}(r/b; m, St_\theta)|$, as a function of cross-stream coordinate r/b at representative streamwise locations

$x/D = 4, 6$, and 8, respectively. In each case the value of St_θ corresponds to that associated with the local maximum in the associated eigenvalue spectrum (e.g. figure 21). The eigenmode shape is presented for several selected representative azimuthal mode numbers in figure 23. It can be seen that the cross-stream variation of $|\varphi^{(1)}(r/b; m, St_\theta)|$ is distinctly different for axisymmetric and helical modes. For instance, at each x/D location, the axisymmetric mode ($m = 0$) exhibits two maxima: a primary one on the jet centreline and a smaller one near $r/b = 1.1$. In contrast, the helical modes each exhibit a minimum on the jet centreline and a single maximum in the jet shear layer. While the exact r/b location of the maximum depends on the azimuthal mode number, all are located on the high-speed side of the shear layer ($r/b \leqslant 1$).

4.5. *POD eigenmode projection onto instantaneous local flow field realizations*

Each of the POD modes is known only up to an arbitrary factor of phase. This follows from the fact that the integration in (3.4) is performed in the r-direction with St_D and m as parameters. In general, the PODmodes are ambiguous in phase for all homogeneous directions, as described in Lumley (1970). The phase information required for a local reconstruction of the flow structure can be restored by the projection of the POD modes onto instantaneous flow field realizations $u_\alpha(r, \theta, t)$ obtained at selected streamwise stations. One approach to doing this would be to use a technique similar to that employed by Citriniti & George (2000) in the axisymmetric shear layer. This method utilized a large array of 138 single sensor probes in the plane $x/D = 3$ to capture the instantaneous streamwise-component flow. However, this was impractical for the acquisition of multi-component realizations of interest in this study. Instead, the approach to be described below uses the *complementary technique* developed by Bonnet *et al.* (1994) in which linear stochastic estimation (LSE) provides the required instantaneous flow field realizations with a sparse array of multi-sensor probes. In particular, the effective interpolation provided by LSE is used to reduce the required number of X-wire probes in the inhomogeneous radial direction. This is similar to the approach taken by Gordeyev & Thomas (2002) in their investigation of large-scale structure in the planar turbulent jet.

4.5.1. *Linear stochastic estimation*

The LSE method, first proposed by Adrian (1977, 1979), estimates a flow field $\boldsymbol{u}(\boldsymbol{x}, t)$ conditioned upon knowledge of the flow $\boldsymbol{u}' \equiv \boldsymbol{u}(\boldsymbol{x}', t')$ at some selected points in space and/or time. For a comprehensive review of the implementation of LSE in turbulent flow the reader is referred to Adrian (1994). Application of the LSE to obtain instantaneous realizations of the flow in the similarity region of a planar turbulent jet for the purpose of POD eigenmode projection is described in some detail by Gordeyev & Thomas (2002).

In the axisymmetric jet the instantaneous local flow field is estimated by utilizing a sparse cross-stream (r, θ) array of 16 X-wire probes. The location of the probes in the crossflow plane is shown schematically in figure 24. As indicated, there are four probes located at $r = 6.35$ mm, separated azimuthally by 90°, and twelve probes located at $r = 25.4$ mm, separated azimuthally by 30°. The innermost radial position corresponds to $0.22 \leqslant r/b \leqslant 0.18$ over the streamwise range $3 \leqslant x/D \leqslant 8$, respectively. Similarly, the outermost radial location corresponds to $0.9 \leqslant r/b \leqslant 0.7$ over the same streamwise range. Such an arrangement allows resolution of azimuthal modes up to $m = 6$ as well as capturing structure near the centre of the jet. The probe sensors were oriented so as to simultaneously measure either the instantaneous (u, v) or (u, w)

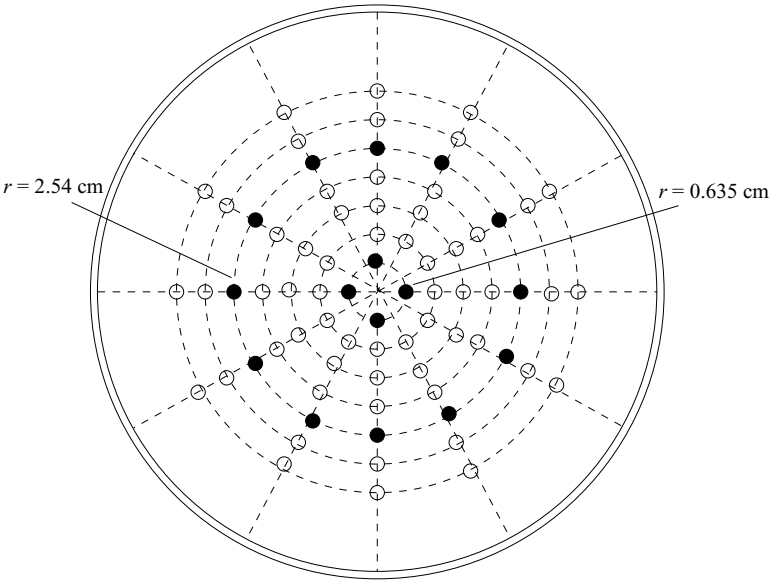

FIGURE 24. Schematic of the measurement grid for the instantaneous flow field measurement for POD projection. Filled circle indicates the probe location.

velocity components. By inserting an additional probe at any given (r, θ) location in the crossflow plane, the ability of LSE to capture the local instantaneous flow field at the corresponding position could be directly assessed. Comparison of numerous sample velocity time-series obtained by direct measurement and by LSE interpolation revealed good agreement. The r.m.s. computed from a given LSE interpolated signal was, in the worst case, within 90 % of the corresponding directly measured value. Representative sample time-series obtained vie LSE interpolation and by direct hot-wire measurement are compared in figure 25.

4.5.2. *Method of POD mode projection*

The procedure that was used for POD mode projection may be described in the following seven steps:

(*a*) The Fourier transform in time of the measured velocity fluctuation is calculated, $\widehat{u}_\alpha(r', \theta, f) = FT\{u_\alpha(r', \theta, t)\}$.

(*b*) Using the LSE method, the velocity field is estimated at all (r, θ)-locations that are marked by the unfilled circles in figure 24: $\widehat{u}_\alpha(r'; \theta, f) \longrightarrow \widetilde{\widehat{u}}_\alpha(r; \theta, f)$. Here the linear stochastic estimation is denoted by $\sim$.

(*c*) The spatial Fourier transform in the θ-direction is performed, $\widetilde{\widehat{u}}_\alpha(r; \theta, f) \longrightarrow \widetilde{\widehat{u}}_\alpha(r; m, f)$.

(*d*) Using the orthogonality property of the POD modes, the POD coefficients (in Fourier space) $a^{(n)}(m, f)$ can be computed by projecting the PODmodes onto an instantaneous realization,

$$a^{(n)}(m, f) = \int \widetilde{\widehat{u}}_\alpha(r, m, f)\varphi_\alpha^{(n)*}(r; m, f) r \, \mathrm{d}r. \tag{4.7}$$

(*e*) The Fourier transform of each POD mode can be restored,

$$\widetilde{\widehat{u}}_\alpha^{(n)}(r, m, f) = a^{(n)}(m, f)\varphi_\alpha^{(n)}(r, m, f). \tag{4.8}$$

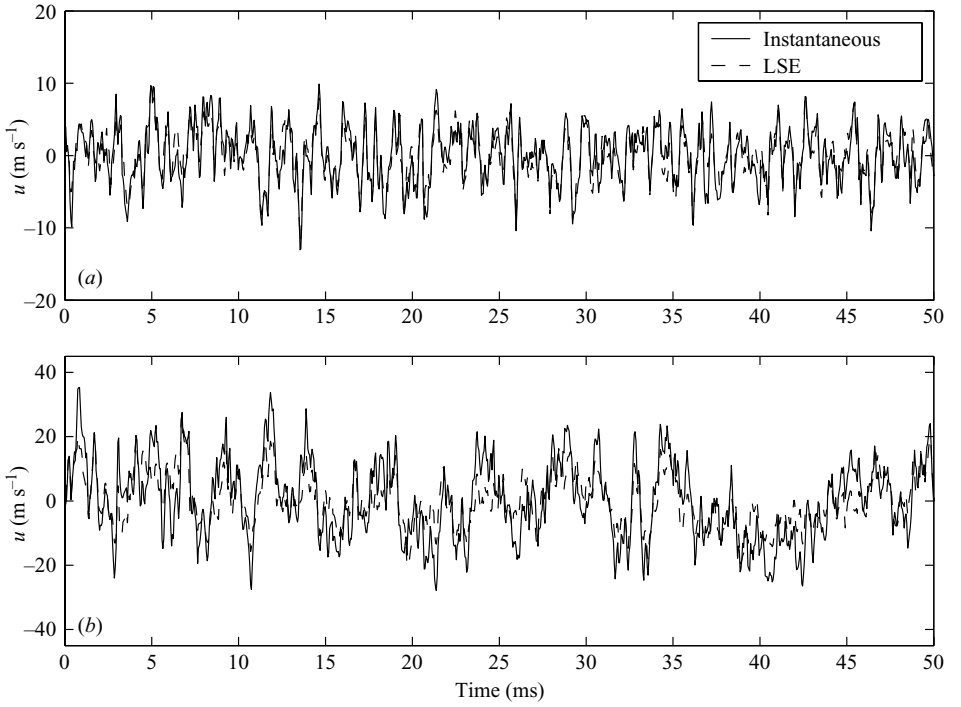

FIGURE 25. Comparison of the streamwise fluctuating velocity component computed from LSE with that directly measured at (*a*) $x/D = 3$, $r/b = 1.12$, (*b*) $x/D = 6$, $r/b = 1.02$.

(*f*) An inverse Fourier transform in time and the θ-direction provides the POD mode in physical space,

$$u_\alpha^{(n)}(r, \theta, t) = FT^{-1}\left\{\widetilde{\widehat{u}}_\alpha^{(n)}(r, m, f)\right\}. \tag{4.9}$$

(*g*) The fluctuating flow field is then the sum of all POD modes,

$$u_\alpha(r, \theta, t) = \sum_{n=1}^{\infty} u_\alpha^{(n)}(r, \theta, t). \tag{4.10}$$

In the sections that follow, results are presented from projections of POD mode 1 onto instantaneous two-component local realizations involving either the measured (u, v) or (u, w) velocity fluctuation time-series in local crossflow $(r - \theta)$ planes.

4.5.3. *POD mode 1, u-component projections*

As noted previously, local POD mode-1 projections using only the streamwise fluctuating component have been presented by both Jung *et al.* (2004) and Citriniti & George (2000). In order to form a basis for comparison with these previous studies, projections of the first POD eigenmode onto the two-component instantaneous flow in local crossflow planes will be presented in this section. These were obtained at several representative x/D locations in the near field of the jet. Results for the streamwise component were obtained by projection of POD mode 1 onto either local (u, v) or (u, w) time-series. In general, u-component projections from both approaches exhibit similar dynamics. The u-component projections to be presented in this section are

based upon a two-component implementation utilizing (u, v) time-series and may be considered as representative of the other cases as well.

Based on the POD mode-1 projection, animations showing the dynamic behaviour of the u-component velocity in the (r, θ)-plane were obtained. In these animations, the instantaneous streamwise velocity associated with POD mode 1 is presented as a surface in the local (r, θ)-plane. Averages over multiple sequential animation frames gave a null result indicating no preferred azimuthal direction (as expected from a properly designed experiment).

Figure 26 presents representative sample frames obtained from the animations at $x/D = 3$, 5 and 7. This figure also serves to illustrate the streamwise evolution in azimuthal mode content of the POD mode-1 u-component fluctuations. The animation frames show that peak fluctuations tend to occur on the high-speed side of the shear layer just inside $r/b = 1$. In general, the animation frames at a given x/D location show a complex pattern indicating the presence of multiple azimuthal modes, and this pattern exhibits significant temporal variation. However, examination of a given sequence of frames indicated that certain azimuthal modes would occur more frequently at a given streamwise location. These preferred azimuthal modes are shown in figure 26. For example, consistent with figure 16, most frames at $x/D = 3$ indicate significant azimuthal mode content for $m = 4$,5 and 6. The sample frame in figure 26 clearly shows the presence of azimuthal mode 5 at $x/D = 3$. Similarly, frames shown in figure 26 for $x/D = 5$ reveal the dominance of azimuthal mode $m = 3$. It is apparent that the higher azimuthal mode content that characterized upstream locations is gone. This reduction in preferred azimuthal mode number with streamwise distance continues, as shown in the sample frames obtained at $x/D = 7$ which clearly show the presence of azimuthal mode 2. In general, these local u-component projections confirm the change in azimuthal mode content of the first POD mode with streamwise distance observed in figure 16 but also show that significant temporal variation occurs at each streamwise location.

From their projection of POD mode 1 on the streamwise component, both Citriniti & George (2000) and Jung *et al.* (2004) observed an energetic transient event that they characterize as a 'volcano-like' eruption of the jet core flow. The eruption forces high-velocity fluid through the centre of the jet while an azimuthal mode $m = 6$ structure appears and is sustained outside the jet core. This behaviour was also observed in the current experiment. In particular, POD mode-1 animations obtained at $x/D = 3$ intermittently showed the occurrence of these events. While these events are relatively common at $x/D = 3$, they occurred much less frequently at $x/D = 4$ and are virtually non-existent by $x/D = 5$. Hence they appear associated with the axisymmetric shear layer development well upstream of the tip of the jet potential core. It appears likely that this event may actually be a manifestation of the localized pairing of axisymmetric jet shear layer vortices with the azimuthal $m = 6$ structure associated with streamwise braids connecting primary toroidal shear layer vortices. More evidence of this topology will be presented in the discussion section of the paper.

4.5.4. *POD mode 1, w-component projections*

From the projection of POD mode 1 onto local two-component (u, w) realizations, animations of the azimuthal w-component fluctuations in local (r, θ) crossflow planes were obtained at several representative x/D locations. As was the case for the u-component, these are presented as surfaces in the local (r, θ)-plane. Figure 27 presents representative sample frames obtained from w-component animations at

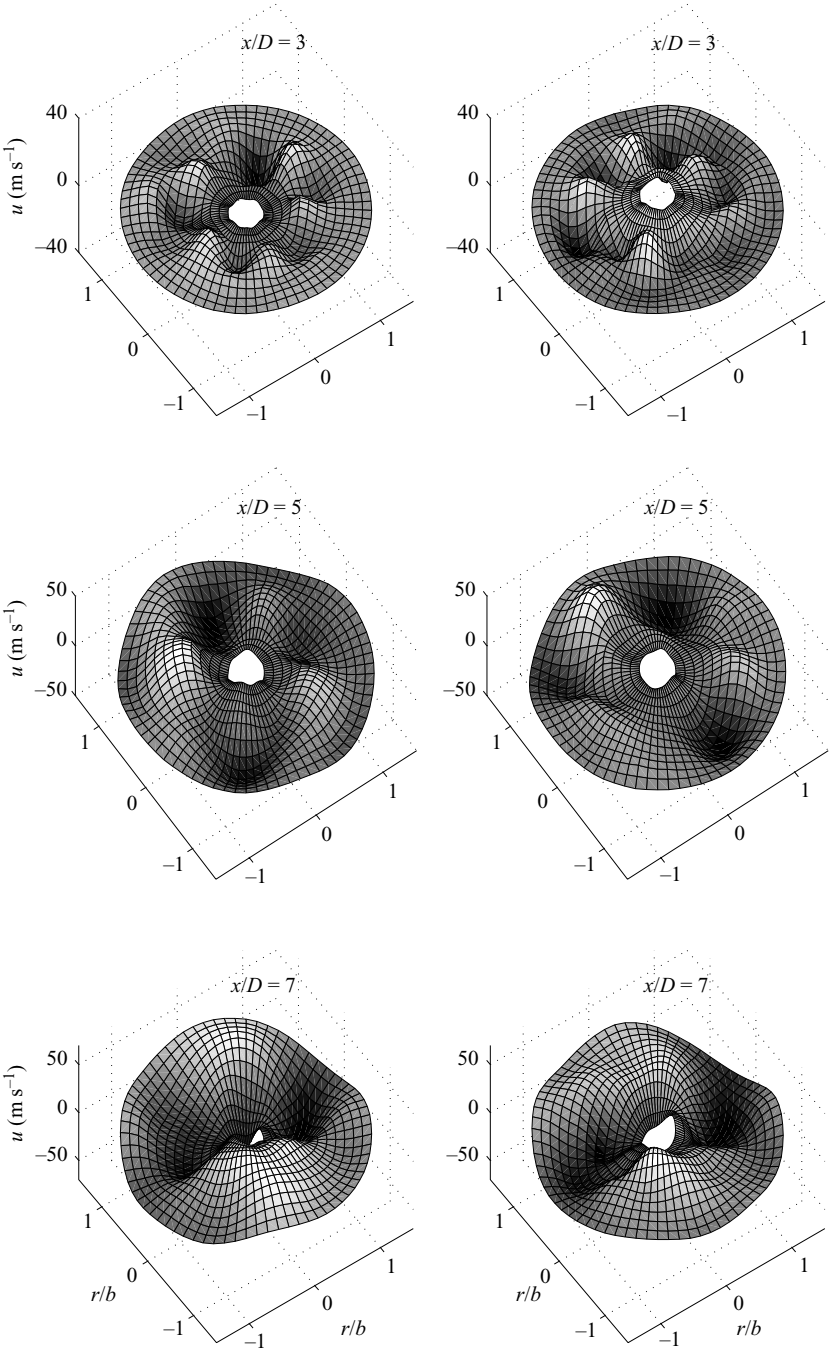

FIGURE 26. Two sample POD mode-1 u-component realizations at representative x/D locations.

$x/D = 3$, 5 and 7. Examination of the w-component frames revealed the presence of multiple azimuthal mode content and considerable local temporal variation. However, consistent with the w-component azimuthal mode energy distributions shown in

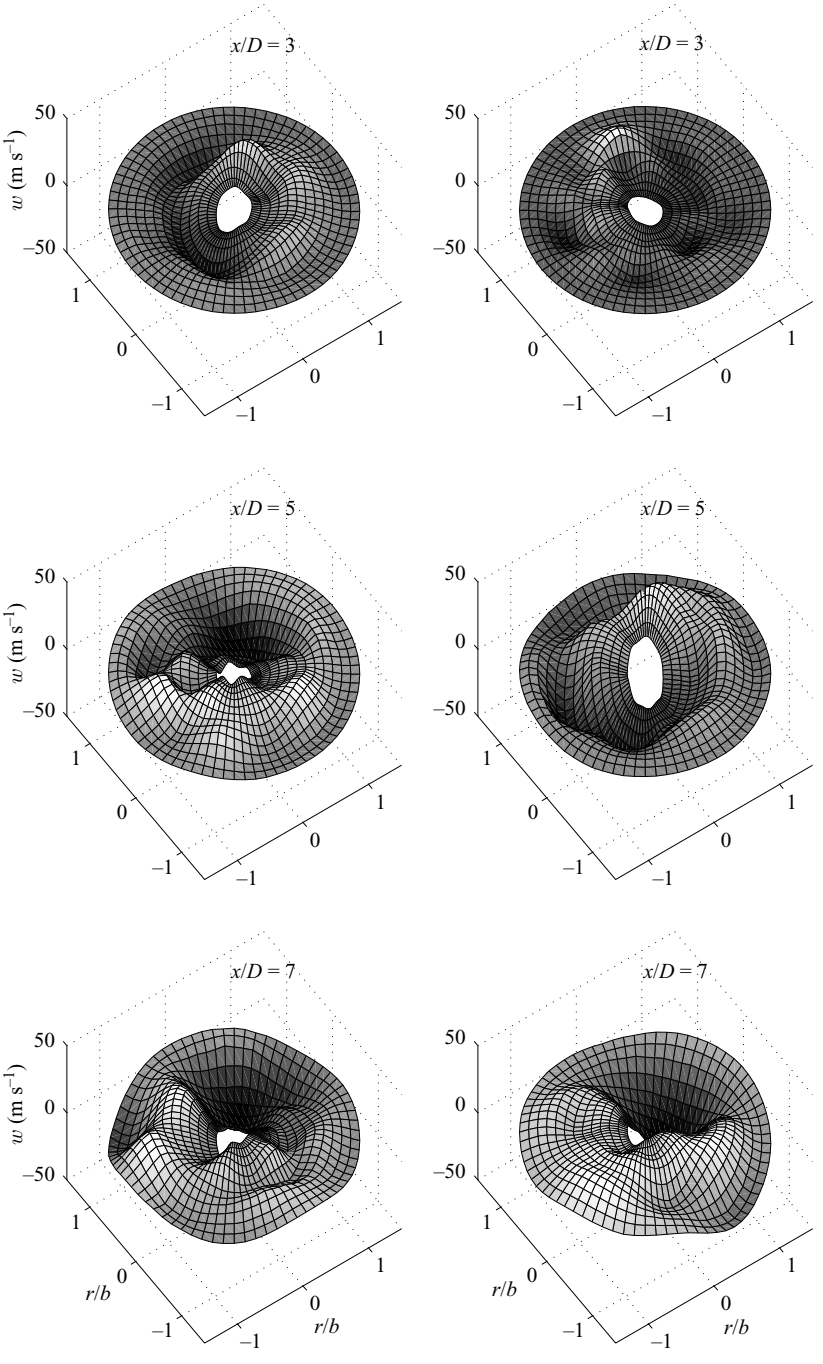

FIGURE 27. Two sample POD mode-1 w-component realizations at representative x/D locations.

figure 18, the animation frames show the strong presence of azimuthal mode $m = 1$ at each x/D location. Note that, in each of the sample frames shown in figure 27, although there is clearly multiple azimuthal mode content, azimuthal mode $m = 1$ is quite prominent. That is, the w-component fluctuation has a strong antisymmetric

component. Figure 27 shows that the dominance of mode $m = 1$ relative to the other azimuthal modes clearly grows with streamwise distance.

The demonstrated dominance of azimuthal mode $m = 1$ for the POD mode-1, w-component combined with its very significant energy content in relation to the u-component (as shown in figure 17) may explain why the vector implementation of the POD shows the local dominance of azimuthal mode $m = 1$ in contradiction to scalar implementations that utilize only the u-component.

4.5.5. *POD mode 1, v-component projections*

Projection of POD mode 1 onto local two-component (u, v) realizations provided animations of the v-component in local (r, θ) crossflow planes. These were obtained at several x/D locations throughout the near field of the jet. As was the case for the w-component, the radial fluctuating component of POD mode 1 is presented as a surface in local (r, θ)-planes. Examination of the resulting v-component animation frames demonstrates a predominantly axisymmetric character of the v-component initially. This is clearly shown in figure 28 which presents sample frames obtained at $x/D = 3$, 5 and 7. Note the dominance of azimuthal mode $m = 0$ for $x/D = 3$ and 5. The axisymmetric character of the POD mode-1 v-component motions is gradually lost with increased x/D. Beyond the tip of the jet core the azimuthal content of the v-component fluctuations becomes dominated by $m = 1$. This is clearly seen in the two frames obtained at $x/D = 7$ shown in figure 28. The results of figure 28 are consistent with the v-component azimuthal mode energy distributions shown previously in figure 19.

The v-component motions associated with the previously described eruption of the jet core flow observed in u-component animations at $x/D = 3$ were examined. This showed that in the first stage of this transient event, the v-component motions are directed radially inward, which leads to the streamwise accelerated core flow. Near the end of the event, the radial component is clearly directed primarily outward. As suggested by figure 19, these POD mode-1 v-component motions appear to be axisymmetric in nature at $x/D = 3$.

5. Discussion

The POD eigenvalue spectra resulting from the three-component implementation of the POD (figure 12) exhibit a remarkable variation over the streamwise range $3 < x/D < 12$. In particular, energy is initially distributed rather broadly over a wide range of resolved azimuthal mode numbers, m, and for $St_D < 0.5$. However, the experiments clearly demonstrate the preferred growth of lower azimuthal mode numbers with increasing streamwise distance, particularly azimuthal modes $m = 1$ and 2. In contrast, the axisymmetric mode $m = 0$ is neutral. When integrated with respect to Strouhal number (temporal frequency), it becomes clear that azimuthal mode $m = 1$ is actually dominant at each x/D location for both POD modes 1 and 2. The dominance of the $m = 1$ mode relative to other azimuthal modes grows with streamwise distance. This result is consistent with results of linear stability theory applied to the local mean velocity profile (e.g. Cohen & Wygnanski 1987). In order to rule out the possibility of the spatial aliasing of azimuthal modes, the experiments were repeated at twice the azimuthal resolution ($\Delta\theta = 7.5^\circ$) which allowed azimuthal modes $m = 0 \ldots 23$ to be resolved. Comparison with the original experiments showed excellent agreement for the most energetic azimuthal modes that form the focus of this paper. Only modes $m \geqslant 7$ exhibited spatial aliasing. Hence, it is conclusively

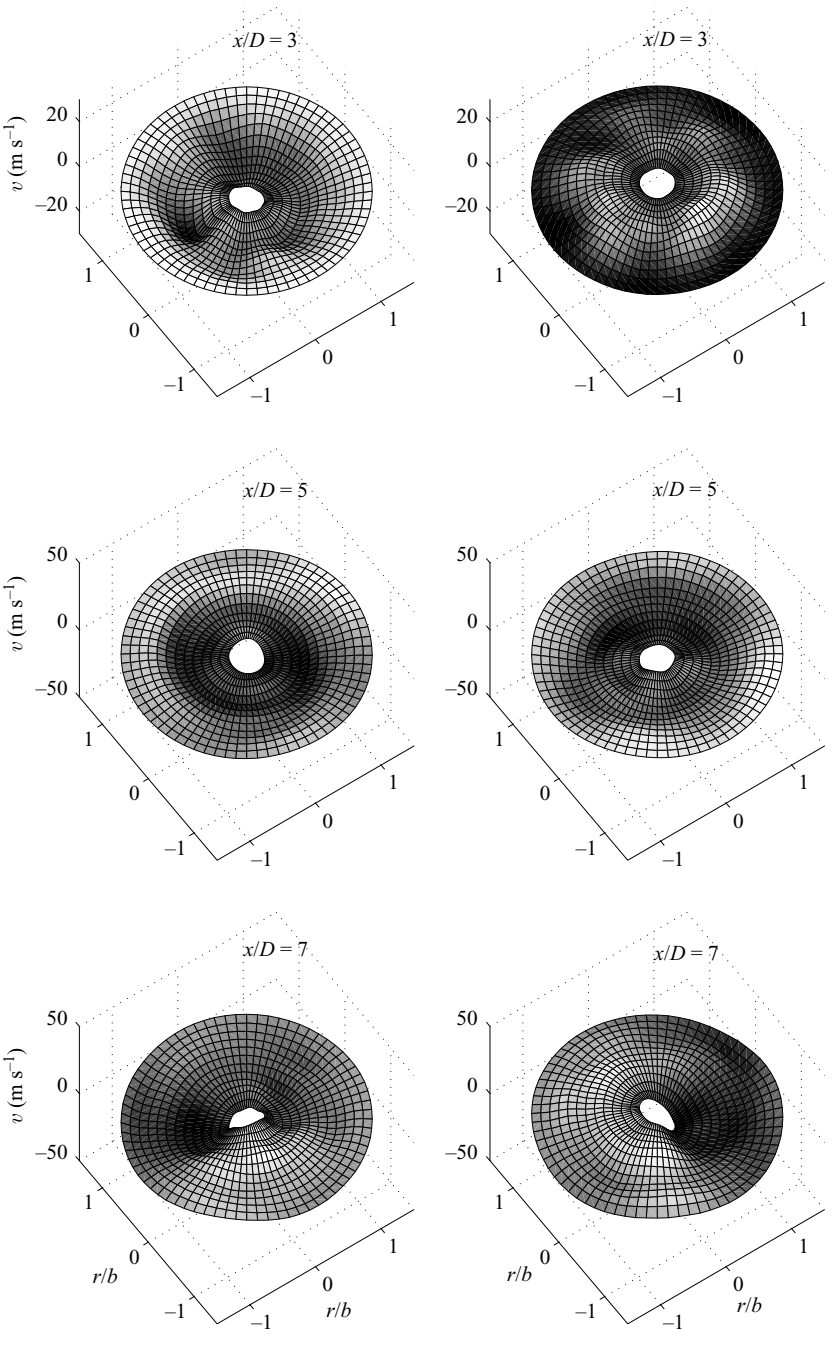

FIGURE 28. Two sample POD mode 1, v-component realizations at representative x/D locations.

demonstrated that the dominance of the $m = 1$ azimuthal mode in the near field of the jet is not related to spatial aliasing.

During the preparation of a revised version of this paper, the authors became aware of a vector implementation of the POD in the far field of the axisymmetric

jet ($x/D = 60$, 70 and 100) by Wänström, Geore & Meyer. This study, which utilized stereo particle image velocimetry, clearly showed the dominance of azimuthal mode $m = 1$ in the far field of the jet, consistent with the results of this study.

The scalar implementation of the POD (using only the u-component) by Jung *et al.* (2004) demonstrated the dominance of azimuthal mode $m = 2$ beyond the tip of the jet core and even into the jet far field. This result does not contradict the results of the current study. As shown in figure 16, an equivalent scalar POD implementation utilizing only the diagonal component Φ_{uu} of the cross-spectral tensor is in excellent agreement with the experimental results of Jung *et al.* (2004) in terms of the locally dominant azimuthal mode numbers. Hence, the scalar u-component implementation of the POD in this study also shows the dominance of azimuthal mode $m = 2$ beyond the tip of the jet core. This comparison also reveals that the azimuthal grid resolution used in the current study is sufficient to faithfully capture the dominant azimuthal modes. Only comparatively low-energy azimuthal modes $m \geqslant 7$ are aliased.

Similar scalar implementations of the POD utilizing either the azimuthal, w, or radial, v, velocity components were performed and these show quite different distributions of energy with azimuthal mode number. For example, the azimuthal component shows the dominance of mode $m = 1$ throughout the initial region of the jet. In contrast, the radial component is initially primarily axisymmetric: $m = 0$ with the first helical mode $m = 1$ becoming significant only near the tip of the jet core.

The energy content of the azimuthal and radial components of the POD modes is shown to be quite significant in relation to the streamwise component energy. For example, for POD mode 1, the energy in the azimuthal component varies from 53 % to 59 % of that in the streamwise component (depending on the streamwise location). Similarly, the radial component accounts for 30–36 %.

The demonstrated dominance of azimuthal mode $m = 1$ for the w-component POD modes 1 and 2, combined with their significant energy content in relation to the u-component may explain why the vector implementation of the POD shows the dominance of azimuthal mode $m = 1$ in the near field of the jet in contradiction to scalar implementations of the POD that utilize only the u-component.

The POD eigenvalue spectra each exhibit a broad spectral peak that is found to occur at a constant value of St_θ for a given azimuthal mode number, m. For fixed azimuthal mode number m, the value of St_θ associated with the eigenvalue spectral peak is constant irrespective of POD mode number, n. However, higher azimuthal mode numbers are associated with lower values of St_θ at peak amplitude. For example, azimuthal modes $m = 0, 1, 2, 3$ correspond to eigenvalue spectral peaks at $St_\theta = 0.048, 0.035, 0.025, 0.013$, respectively (independent of POD mode number). Note that these values of St_θ vary linearly with azimuthal mode number. The scaling of eigenspectra peaks with constant St_θ is consistent with the notion that the dominant POD modes are a manifestation of modes of instability of the turbulent axisymmetric shear layer. The scaling of the eigenvalue spectra with St_θ breaks down for streamwise locations downstream of the jet core as one would expect. Presumably, scaling eignespectra peak frequencies by the local jet mean velocity half-width and maximum velocity would lead to a constant Strouhal number as in the planar jet study by Gordeyev & Thomas (2000), although this far-field behaviour was not investigated in the current study.

The POD eigenmode-1 cross-stream shape functions are distinctly different for axisymmetric and helical modes. The axisymmetric mode possesses a maximum on the jet centreline and a smaller peak near the centre of the jet shear layer. In contrast, the helical modes possess zero amplitude on the jet centreline and a single peak

located on the high-speed side of the jet shear layer ($r/b < 1$). The peak cross-stream location depends on the azimuthal mode number.

Projection of POD mode 1 onto two-component instantaneous realizations of the flow, (either (u, w) or (u, v)), obtained in local (r, θ) crossflow planes allows the local dynamic behaviour of the jet coherent structure to be examined. The local instantaneous realizations were obtained by using the complementary technique of Bonnet *et al.* (1994). Projections of POD mode 1 were found to exhibit considerable temporal variation in azimuthal mode content at a given streamwise location. In general, the azimuthal mode content of a given animation frame typically involved multiple modes. Examination of the sequence of frames at a given x/D location clearly revealed that certain azimuthal modes were 'preferred' in terms of both frequency of occurrence and amplitude. Several example frames showing local preferred azimuthal modes have been presented in this paper. Examination of the animation frames make it clear that modes $m = 5, 6$ more typically dominate the POD mode-1 u-component near $x/D = 3$ and that mode $m = 2$ tends to dominate farther downstream with a gradual variation at locations in between. The observed dynamic behaviour associated with the u-component was similar whether based on the (u, v) or (u, w) projections.

Based on projection of POD mode 1 onto instantaneous (u, w) time series, the azimuthal POD mode-1 motions were examined. Examination of the w-component frames revealed the strong presence of azimuthal mode $m = 1$ at each x/D location. That is, although there is temporal variation and multiple azimuthal mode content in the frame sequence, the POD mode-1,w-component fluctuation possesses a strong antisymmetric component. This observation is consistent with the w-component azimuthal mode energy distributions shown in figure 18. The v-component (radial) POD mode-1 motions were found to be primarily axisymmetric in nature at locations upstream of the tip of the jet potential core. The v-component POD mode-1 motion was also found to play a key role as a precursor of intermittent core flow acceleration events, first noted by Citriniti & George (2000). For streamwise locations closer to the end of the jet core, the azimuthal symmetry in the v-component motions is lost and animation frames clearly show the presence of azimuthal mode $m = 1$.

In order to correctly compute the phase coefficient $a^{(n)}(m, f)$ in equation (4.7), the u-, v- and w-components must be acquired simultaneously. Unfortunately the X-wires provide only simultaneous (u, v) or (u, w) velocity fluctuation time-series (depending on their orientation in the flow). Neglect of one of the velocity components will result in lost phase information since $a^{(n)}(m, f) = a_u^{(n)}(m, f) + a_v^{(n)}(m, f) + a_w^{(n)}(m, f)$ where

$$a_\alpha^{(n)}(m, f) = \int \widetilde{\widehat{u}}_\alpha(r, m, f)\varphi_\alpha^{(n)*}(r; m, f) r \, \mathrm{d}r \text{ (no summation on } \alpha). \tag{5.1}$$

In order to gauge the loss of phase information associated with the neglect of either $a_v^{(n)}(m, f)$ or $a_w^{(n)}(m, f)$, the ratios of the norms of the phase coefficients, $|a_v^{(n)}|/|a_u^{(n)}|$ and $|a_w^{(n)}|/|a_u^{(n)}|$, for the first POD mode were computed from the two groups of measurements, (u, v) and (u, w). Figure 29 shows a comparison of the ratios $|a_v^{(1)}|/|a_u^{(1)}|$ and $|a_w^{(1)}|/|a_u^{(1)}|$ for the dominant azimuthal mode numbers $m = 1$ and $m = 2$ at two representative streamwise stations. For the range of Strouhal number $(0 \leqslant St_D \leqslant 0.5)$ at $x/D = 3$, the size of $|a_w^{(1)}|/|a_u^{(1)}|$ is greater by at least a factor 3 than $|a_v^{(1)}|/|a_u^{(1)}|$. This difference increases with streamwise distance as is apparent from figure 29(b). Hence, this result suggests that if a velocity component must be neglected, then neglect of $a_v^{(n)}(m, f)$ will yield minimum error in the reconstruction of the flow field mode-1 coherent structure in physical space. This is particularly true for x/D locations near and beyond the tip of the jet core.

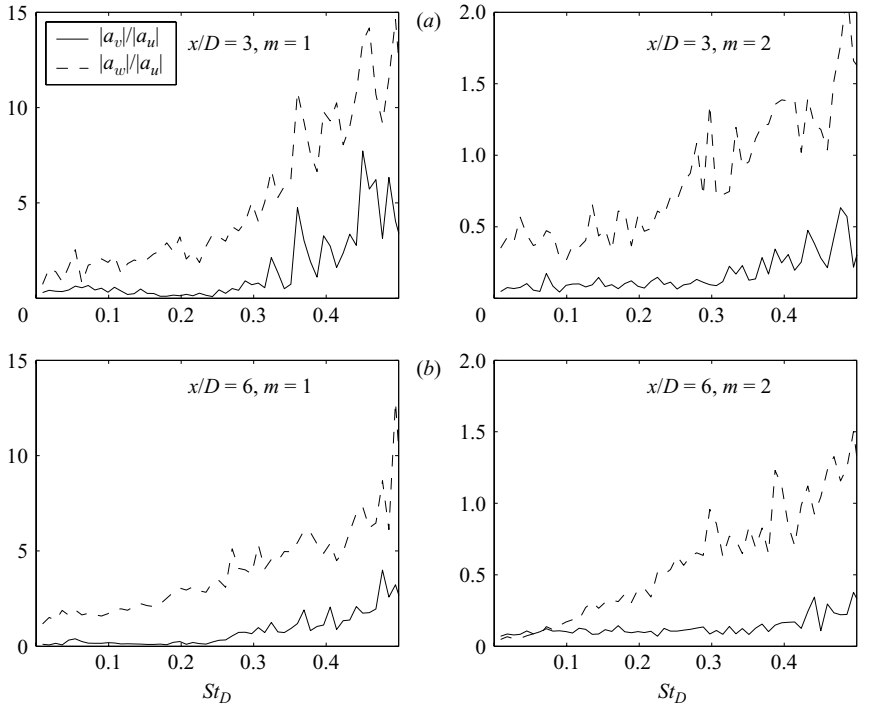

FIGURE 29. Ratio of the norms of phase coefficients for azimuthal mode number $m = 1$ and $m = 2$ at two representative streamwise locations: (*a*) $x/D = 3$, (*b*) $x/D = 6$.

It is common to use a triple decomposition of the velocity field in order to account for the presence of coherent structure in the flow (e.g. Hussain 1986),

$$\boldsymbol{u} = \bar{\boldsymbol{U}} + \boldsymbol{u}_{ls} + \boldsymbol{u}_{fs} \tag{5.2}$$

where $\bar{\boldsymbol{U}}$ is the mean velocity, $\boldsymbol{u}_{ls}$ represents the large-scale structure and $\boldsymbol{u}_{fs}$ is the fine-scale, phase incoherent turbulence. In a similar manner, the resolved flow structure in the axisymmetric jet may be represented as a summation of the dominant POD modes,

$$\boldsymbol{u}_{resolved} = \sum_{n=1}^{N} \boldsymbol{u}^{(n)}. \tag{5.3}$$

Since the focus is on the large-scale motions, those that do not contribute to the cross-spectral tensor, $\boldsymbol{u}_{unresolved}$, are considered 'fine-scale' and are neglected. In this sense, the term fine-scale is intimately related to the resolution of the measurements. The large-scale flow structure can then be represented as a series consisting of the sum of the mean flow $\bar{\mathbf{U}}$ and N POD modes $\boldsymbol{u}^{(n)}$. Note that the mean flow is time independent and is thus orthogonal to the POD modes. Motivated by the rapid energy convergence demonstrated by the POD eigenvalues, as a first approximation to the large-scale jet structure we have

$$\boldsymbol{u}_{struc} = \bar{\boldsymbol{U}}(r) + \boldsymbol{u}^{(1)}. \tag{5.4}$$

Further, owing to the results shown in both figures 17 and 29, the u- and w-component POD modes are used to reconstruct the jet large-scale structure. Since, we are interested in only the most basic aspect of the jet large-scale structure topology,

the error in neglecting the v-component would hardly alter its principal shape. Only for comparative purposes at the most upstream x/D location is a reconstruction presented utilizing the u- and v- components.

An approximation is made that the flow is effectively parallel in the streamwise direction at the x/D locations where the POD mode projections are made. The local reconstructions of the flow are presented in a frame of reference convecting with the structure. Hence, we present the structure in a frame of reference moving with convective speed, $U_c = 0.6U_m$ which is approximately independent of r. In a frame of reference moving downstream at speed U_c, new variables are then defined as $x \to x - U_c t$, $r \to r$, $\theta \to \theta$, and $u \to u - U_c$. One way to present the resulting flow structure would be to simply present the velocity field, $u - U_c$, as a function of r, θ and pseudo-spatial streamwise coordinate, $x = -U_c t$. Instead of this approach, the large-scale structure will be visualized by means of the so-called $-\lambda_2$ surface which Jeong & Hussain (1995) have shown to be an objective criterion for eddy structure identification (not to be confused with the notation used in the current paper for POD eigenvalue). This technique is based on the detection of local pressure minima associated with vortex cores.

Figure 30 presents sample flow field reconstructions obtained at $x/D = 3$ based on both (u, v) and (u, w) POD mode-1 projections. In each case the $-\lambda_2 = 3\,\%$-of-maximum iso-surface is used to visualize the underlying large-scale flow structure in the convected frame of reference. By selectively filtering the azimuthal mode numbers m included in the realizations, one can investigate the underlying flow topology involved. In figure 30(a), both of the (u, w) realizations are identical but different azimuthal mode filtering has been applied. Similarly, the pair of (u, v) realizations in figure 30(b) are identical. Both of the realizations on the right-hand side of the figure include only the azimuthal modes $m = 0$ and $m = 5$. These clearly show the presence of a sequence of toroidal shear-layer vortices. The $m = 5$ structure is associated with streamwise vortical braids that appear to connect these primary shear layer vortices. The (u, v)-based structural realization shown on the right of figure 30(b) also shows two axisymmetric vortices that have just undergone merging.

On the left hand side of figure 30 the reconstructions are filtered to include only azimuthal modes $m = 0$ and $m = 1$. These show that even at $x/D = 3$, the jet is beginning to develop an underlying helical vortical structure. It was found that, consistent with the v- and w-component azimuthal mode energy distributions shown previously in figures 19 and 18, respectively, the (u, w)-component-based flow reconstructions more clearly showed the helical structure in the jet.

Figure 31 presents local flow field reconstructions base upon the (u, w)-components only. Again, the $-\lambda_2 = 3\,\%$ of-maximum iso-surface is used to visualize the underlying structure. At this x/D location the jet coherent structure is now dominated by a helical vortex. Shown in figure 31 is a realization filtered first to include only mode $m = 1$ and then both azimuthal modes $m = 1$ and $m = 2$. The underlying helical vortical structure is readily apparent. Examination of numerous realizations revealed no preferred orientation for the helical structures (i.e. right- and left-handed were equally likely). Although not shown here, filtering the flow to include the axisymmetric and higher azimuthal modes (like those shown in figure 30) revealed little in the way of organized large-scale structure at this location.

The helical large-scale structure in the axisymmetric jet that is observed in figure 31 is found to persist beyond the tip of the jet core. Figure 32 shows a similar sample (u, w)-based flow field reconstruction obtained at $x/D = 6$. The azimuthal mode filtering is the same as that employed in figure 31. This clearly shows that the local jet

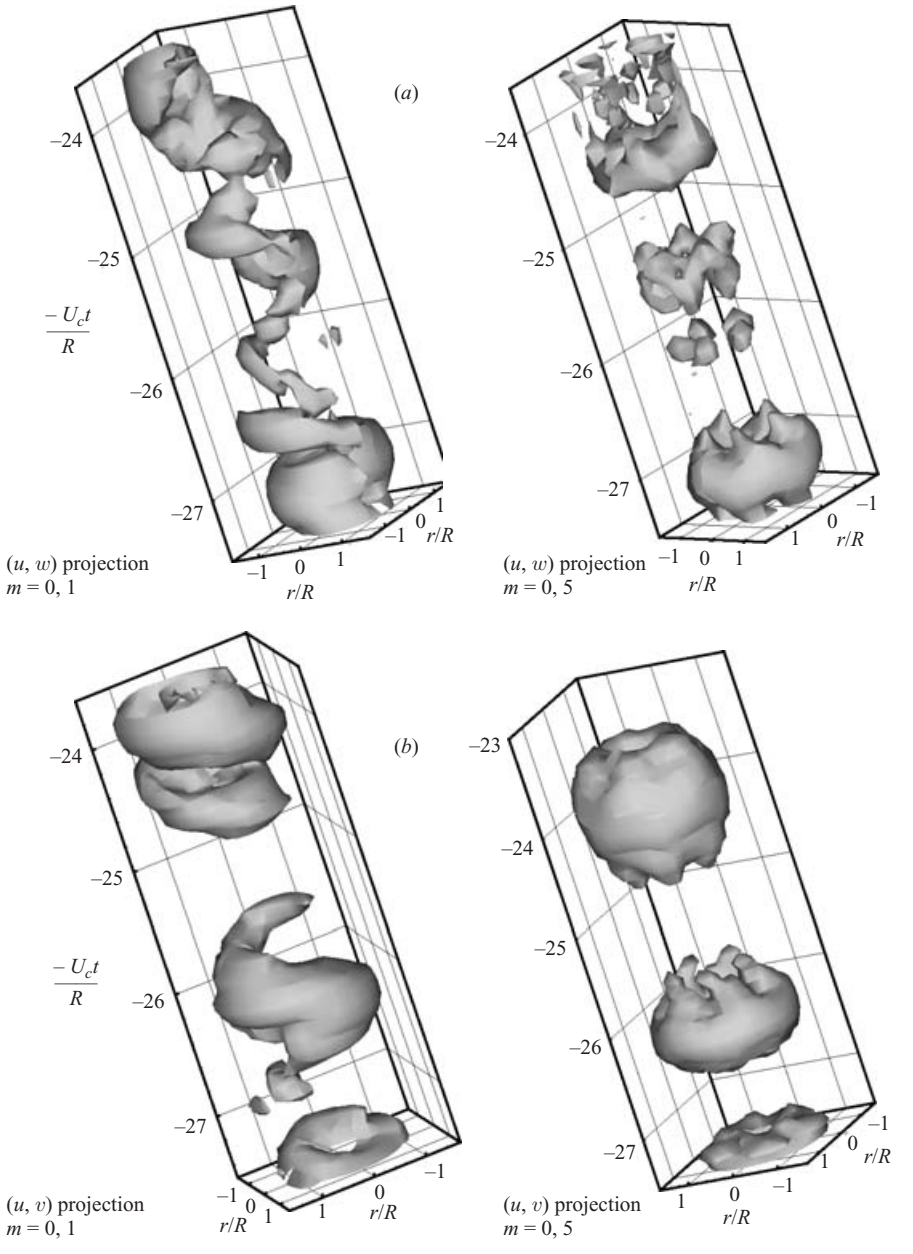

FIGURE 30. $-\lambda_2$ surface at $x/D = 3$ obtained from the projection of the first POD mode.

coherent structure topology beyond the tip of the jet core is dominated by a helical vortex structure. This structure was found to persist to the last measurement station examined in this study and was dominated by azimuthal mode $m = 1$.

This work was initiated under the support of NASA Langley Research Center. This support is gratefully acknowledged. In addition, the authors would like to acknowledge beneficial discussions with Thomas C. Corke, Stanislav V. Gordeyev and William K. George.

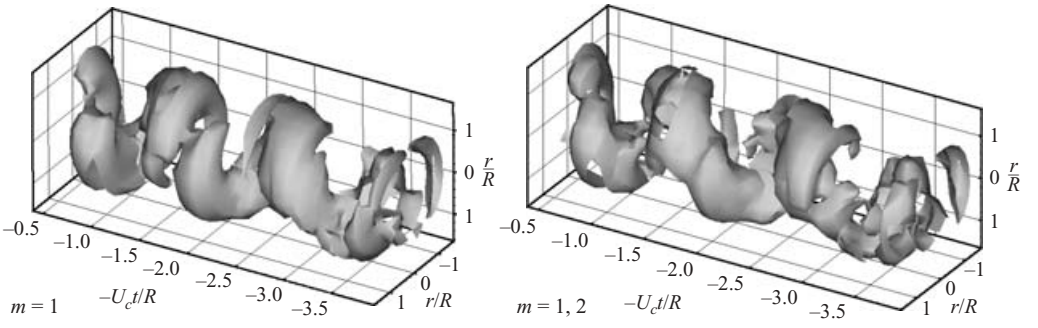

FIGURE 31. $-\lambda_2$ surface at $x/D = 4$ obtained from the projection of the first POD mode, (u, w)-components.

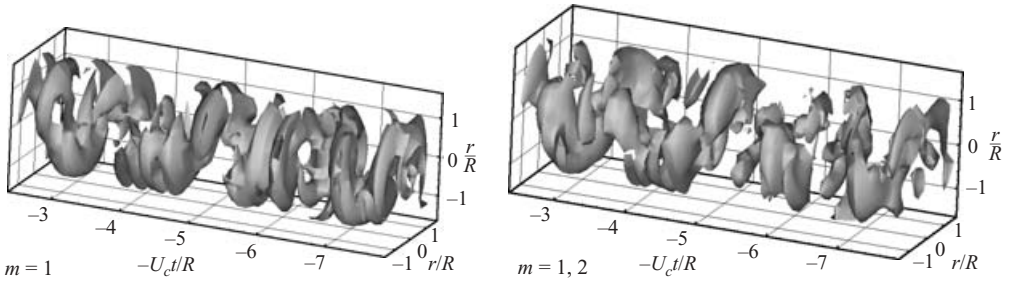

FIGURE 32. $-\lambda_2$ surface at $x/D = 6$ obtained from the projection of the first POD mode, (u, w)-components.

Appendix A. Temporal and spatial aliasing concerns

The acquired velocity time-series data are discrete in both time and space so careful consideration must be given in order to minimize temporal and spatial aliasing. Avoidance of temporal aliasing is straightforward and is considered first. Using a conventional single-sensor hot-wire probe, autospectral density measurements were obtained in the jet at various radial and streamwise locations at a Nyquist frequency of 50 kHz. As an example, figure 33 presents autospectra of the streamwise fluctuating velocity component obtained at $x/D = 3$ for several radial positions in the jet shear layer. From this figure (and similar measurements that are not presented here) it can be seen that most of the fluctuation energy is contained in a frequency band below 10 kHz although the frequency bandwidth does extend to approximately 20 kHz. This indicates that the velocity fluctuations should be sampled at 40 kHz or greater in order to avoid temporal aliasing. However, since the focus of this experiment is on the extraction of large-scale structure in the flow which is investigated via cross-spectral methods, it will be demonstrated that a much lower sampling frequency combined with the use of analogue anti-alias filters offers the best approach.

The cross-spectral measurements in this study were obtained at a sampling frequency of 20 kHz. Converged cross-spectral density functions $S_{\alpha\alpha}(r, r'; f)$ obtained with a sampling frequency of 20 kHz at various locations in the jet show that significant correlation is actually restricted to a much lower frequency band. As an example figures 34 and 35 present $|S_{uu}(r = b, r'; St_D)|$, $|S_{vv}(r = b, r'; St_D)|$ and $|S_{ww}(r = b, r'; St_D)|$ obtained for $b/5 \leqslant r' \leqslant 7b/5$ at the two representative streamwise locations $x/D = 3$ and 6, respectively. Note that in each case there is virtually no

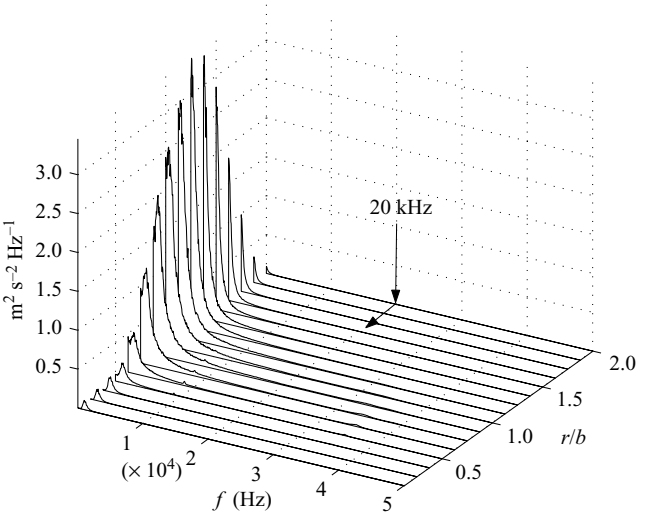

FIGURE 33. u-component autospectra at different radial locations at $x/D = 3$.

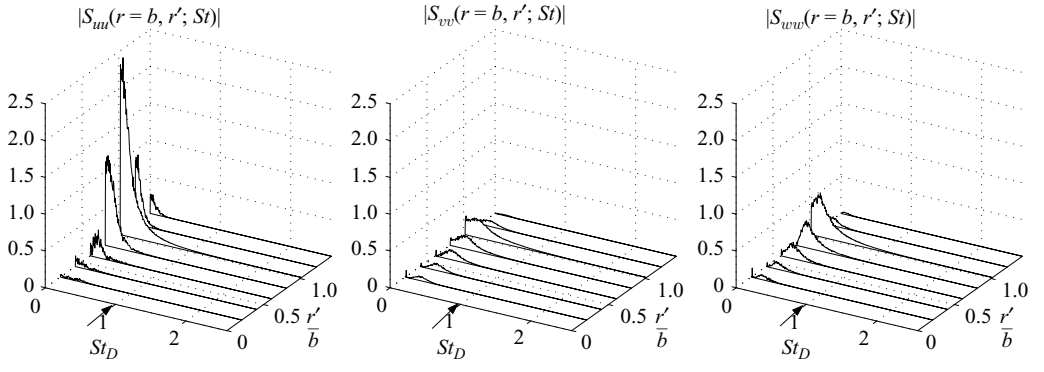

FIGURE 34. Cross-spectral modulus $|S_{uu}(r = b, r'; St_D)|$, $|S_{vv}(r = b, r'; St_D)|$ and $|S_{ww}(r = b, r'; St_D)|$ at $x/D = 3$ for $b/5 \leqslant r' \leqslant 7b/5$.

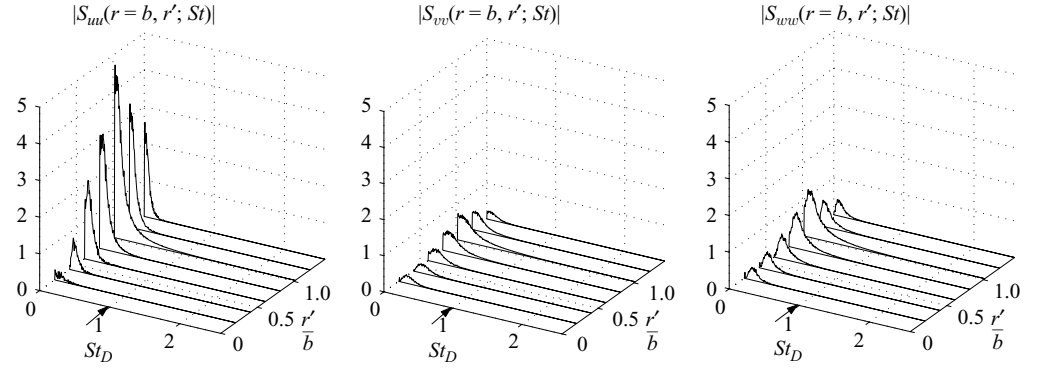

FIGURE 35. Cross-spectral modulus $|S_{uu}(r = b, r'; St_D)|$, $|S_{vv}(r = b, r'; St_D)|$ and $|S_{ww}(r = b, r'; St_D)|$ between two probes at $x/D = 6$ for $b/5 \leqslant r' \leqslant 7b/5$.

spectral coherence for frequencies $St_D > 1$, where $St_D = 1$ corresponds to a temporal frequency of approximately $f = 2.2\,\text{kHz}$. This indicates that spatially coherent structures in the near field of the axisymmetric jet lie at comparatively low frequencies. Therefore, the use of a 10 kHz Nyquist frequency combined with analogue anti-alias filters will both prevent temporal aliasing and provide more than sufficient bandwidth for the two-point cross-spectral measurements.

For the initial POD experiments, the measurement grid was equally spaced in the azimuthal direction with a $\Delta\theta = 15^\circ$ (see figure 9). This corresponded to a resolved azimuthal mode number range of $m = 0 \ldots 11$. Of course, if there are higher azimuthal modes present in the flow, these can be aliased to lower m. In order to assess this, the entire experiment was repeated with $\Delta\theta = 7.5^\circ$ giving a resolved azimuthal mode number range of $m = 0 \ldots 23$. Comparison of the results from the two experiments provides a direct assessment of the degree of spatial aliasing of azimuthal modes. Results from the two experiments are shown in figure 15, which compares the azimuthal mode energy distribution $\xi^{(n)}(m)$ for POD modes 1 and 2 as obtained from both experiments. The results are compared at two representative streamwise locations, $x/D = 3$ and 6. The comparison shown in figure 15 may be considered representative of other streamwise locations as well. This figure clearly shows that only comparatively low-energy azimuthal modes $m \geqslant 7$ are significantly aliased. In fact, the lower, more energetic, azimuthal mode distribution of energy is nearly identical for the two experiments.

The radial coordinate is inhomogeneous and in this direction the flow is expanded in terms of POD eigenfunctions rather than Fourier modes. However, in order to assess the correlated length scales resolved by the rake in the radial direction, it is useful to temporarily think in terms of Fourier modes. To this end, two-point cross-spectra, $S_{uu}(r = 0, r'; St_D)$, were computed between two single-sensor probes; one probe was fixed at the centre of the jet ($r = 0$) and the other was movable in the radial direction r' with a small, fixed increment ($\Delta r = 1.25\,\text{mm}$). Thus, the minimum spacing between probes was approximately 1/5 of the value that was actually used in the POD measurements. The cross-spectral tensor for the streamwise fluctuating velocity component S_{uu} is computed for the movable probe positions $0 < r' < 1$. A spatial Fourier transform of the resulting cross-spectra yields

$$X_{uu}(k_r, r', St_D) = \int S_{uu}(r, r', St_D) \mathrm{e}^{-\mathrm{i}k_r r'}\, \mathrm{d}r'. \tag{A 1}$$

where k_r is a wavenumber in the radial direction. Of particular interest is the value of $|X_{uu}(k_r, r', St_D)|^2$ as a function of $k_r b$ for a representative range of frequencies (not presented here). These show that all significant lateral correlation of streamwise fluctuations occurs for $k_r b < 11.5$ at $x/D = 3$ and for $k_r b < 9$ at $x/D = 6$. This implies that the length scale in the radial direction associated with significant correlation is $\lambda_r \geqslant 0.55b$ at $x/D = 3$ and $\lambda_r \geqslant 0.7b$ at $x/D = 6$. The fixed probe spacing used for the POD measurements ($\Delta r = 6.35\,\text{mm}$) corresponds to maximum resolved radial wavenumber $k_r b = 14.2$ at $x/D = 3$ and $k_r b = 15.4$ at $x/D = 6$. Hence, at all streamwise locations investigated, the fixed radial probe spacing used for the POD measurements is capable of resolving the radially coherent motions associated with the jet large-scale structure.

REFERENCES

Adrian, R. J. 1977 On the role of conditional averages in turbulent theory. In *Turbulence in Liquids: Proc, 4th Biennial Symposium on Turbulence in Liquids* (ed. G. Patteson & J. Zakin), pp. 322–332. Science Press, Princeton.

Adrian, R. J. 1979 Conditional eddies in isotropic turbulence. *Phys. Fluids* **22**, 2065–2070.

Adrian, R. J. 1994 Stochastic estimation of conditional structure: A review. *Appl. Sci. Res.* **53**, 291–303.

Arndt, R. E. A., Long, D. F. & Glauser, M. N. 1997 The proper orthogonal decomposition of pressure fluctuations surrounding a turbulent jet. *J. Fluid Mech.* **340**, 1–33.

Aubry, N., Holmes, P., Lumley, J. L. & Stone, E. 1988 The dynamics of coherent structures in the wall region of the turbulent shear layer. *J. Fluid Mech.* **192**, 115–175.

Bendat, S. J. & Piersol, A. G. 1986 *Random Data,* 2nd Edn. Wiley Interscience.

Berkooz, G., Holmes, P. & Lumley, J. L. 1993 The proper orthogonal decomposition in the analysis of turbulent flows. *Annu. Rev. Fluid Mech.*, **25**, 539–575.

Bonnet, J. P., Cole, D. R., Delville, J., Glauser, M. N. & Ukeiley, L. S. 1994 Stochastic estimation and proper orthogonal decomposition: complementary techniques for identifying structure. *Exps. Fluids* **17**, 307–314.

Bonnet, J. P. & Delville, J. 1996 General concepts on structure identification. In *Eddy Structure Identification* (ed. J. P. Bonnet). Springer.

Bonnet, J. P. & Delville, J. 2001 Review of coherent structures in turbulent free shear flows and their possible influence on computational methods. *Flow, Turbulence Combust*. **66**, 333–353.

Bradshaw, P., Ferriss, D. H. & Johnson, R. F. 1964 Turbulence in the noise-producing region of a circular jet. *J. Fluid Mech.* **18**, 591–624.

Chu, H. C. 1993 An experimental study of nonlinear wave coupling and energy transfer characterizing the transition of a planar jet shear layer. PhD dissertation, University of Notre Dame.

Citriniti, J. H. & George, W. K. 2000 Reconstruction of the global velocity field in the axisymmetric mixing layer utilizing the POD. *J. Fluid Mech.* **418**, 137–166.

Cohen, J. & Wygnanski, I. 1987 The evolution of instabilities in the axisymmetric jet. Part 1. The linear growth of the disurbances near the nozzle. *J. Fuid Mech.* **176**, 191–219.

Crow, S. C. & Champagne, F. H. 1971 Orderly structure in jet turbulence. *J. Fluid Mech.* **48**, 547–591.

Davies, P. O. A. L., Ko, N. M. W. & Bose, B. 1967 The local pressure field of turbulent jets. *Aero. Res. Counc. Paper* **989**.

Delville, J., Ukeiley, L. S., Cordier, L., Bonnet, J. P. & Glauser, M. N. 1999 Examination of large scale structures in a plane mixing layer. Part 1. Proper orthogonal decmposition. *J. Fluid Mech.* **391**, 91–122.

Drubka, R. E. 1981 Instabilities in the near field of turbulent jets and their dependence on initial conditions. PhD Dissertation, Illinois Institute of Technology, Chicago.

Gamard, S., George, W. K. & Jung, D. 2004 Downstream evolution of the most energetic modes in a turbulent axisymmetric jet at high Reynolds number. Part 2. The far-field region. *J. Fluid Mech.* **514**, 173–204.

Glauser, M. N. 1987 Coherent structures in axisymmetric turbulent jet mixing layer. PhD Dissertation, SUNY, Buffalo.

Glauser, M. N. & George, W. K. 1987 Orthogonal decomposition of the axisymmetric jet mixing layer including azimuthal dependence. In *Advances in Turbulence* (ed. J. C. Comte-Bellot *et al.*) Springer.

Glauser, M. N. & George, W. K. 1992 Application of multipoint meassurements for flow characterization. *Expl Thermal Fluid Sci.* **5**, 617–632.

Glauser, M. N., Leib, S. J. & George, W. K. 1987 Coherent structures in axisymmetric turbulent jet mixing layer. In *Turbulent Shear Flows 5* (ed. J. C. Durst *et al.*). Springer.

Gordeyev, S. V. & Thomas, F. O. 2000 Coherent structure in turbulent planar jet. Part 1. Extraction of POD eigenmodes and their self-similarity. *J. Fluid Mech.* **414**, 145–194.

Gordeyev, S. V. & Thomas, F. O. 2002 Coherent structure in turbulent planar jet. Part 2. Structural topology via POD eigenmode projection. *J. Fluid Mech.* **460**, 349–380.

Gutmark, E. & Ho, C. M. 1983 Preferred modes and the spreading rates of jets. *Phys. Fluids* **26**, 2932–2938.

Gutmark, E. & Wygnanski, I. 1976 The planar turbulent jet. *J. Fluid Mech.* **73**, 465–495.

Ho, C. M. & Huang, L. S. 1982 Subharmonics and vortex merging in mixing layers. *J. Fluid Mech.* **119**, 443–473.

Holmes, P., Lumley, J. L. & Berkooz, G. 1996 *Turbulence, Coherent Structures, Dynamical Systems and Symmetry*. Cambridge University Press.

Hussain, A. K. M. F. 1986 Coherent structures and turbulence. *J. Fluid Mech.* **173**, 303–356.

Hussein, H. J., Capp, S. P. & George, W. K. 1994 Velocity measurements in a high-Reynolds-number, momentum conserving, axisymmetric, turbulent jet. *J. Fluid Mech.* **258**, 31–75.

Iqbal, M. O. 2006 Coherent structure in a turbulent axisymmetric jet via a vector implementation of the proper orthogonal decomposition. PhD Dissertation, University of Notre Dame, Notre Dame, IN.

Jeong, J. & Hussain, A. K. M. F. 1995 On the identification of a vortex. *J. Fluid Mech.* **285**, 69–94.

Jung, D., Gamard, S. & George, W. K. 2004 Downstream evolution of the most energetic modes in a turbulent axisymmetric jet at high Reynolds number. Part 1. The near-field region. *J. Fluid Mech.* **514**, 173–204.

Karhunen, K. 1946 'Zur Spektraltheorie Stochasticher. *Prozessa Ann. Acad. Sci. Fennicae* **37**

Kibens, V. 1981 The limit of initial shear layer influence on jet development. *AIAA Paper* 81-1960.

Loéve, M. M. 1955 '*Probability Theory*. Van Nostrand.

Lumley, J. 1967 The structure of inhomogeneous turbulent flows. In *Proc. Intl Colloq. on Fine Scale Structure of the Atmosphere and its Influence on Radio Waves* (ed. A. M. Yaglam & V. I. Tatarsky), pp. 166–178. Doklady Akademii Nauk SSSR, Moscow, Nauka.

Lumley, J. 1970 *Stochastic Tools in Turbulence*. Academic.

Monkewitz, P. A. 1988 Subharmonic resonance, pairing and shredding in the mixing layer. *J. Fluid Mech.* **188**, 223–252.

Tam, C. K. W. 1986 Excitation of instability waves by sound - A physical interpretation. *J. Sound Vib.* **105**, 169–172.

Taylor, J. A., Ukeiley L. S. & Glauser, M. N. 2001 A low-dimensional description of the compressible axisymmetric shear layer. *AIAA Paper* 2001-0292.

Thomas, F. O. 1991 Structure of mixing layers and jets. *Appl. Mech. Rev.* **44(3)**, 119–153.

Tinney, C. E., Glauser, M. N. & Ukeiley, L. S. 2005 The evolution of the most energetic modes in a high subsonic Mach number turbulent jet. *AIAA Paper* 2005-0417.

Ukeiley, L. S., Cordier, L., Manceau, R., Delville, J., Glauser, M. N. & Bonnet, J. P. 2001 Examination of large-scale structures in a turbulent plane mixing layer. Part 2. Dynamical systems model. *J. Fluid Mech.*, **441**, 67–108.

Ukeiley, L. S. & Glauser, M. N. 1995 Dynamics of large-scale structures in a plane turbulent mixing layer. *Rep. MAE*-311. Department of Aerospace and Mechanical Engineering, Clarkson University.

Ukeiley, L. S. & Seiner, J. M. 1998 Examination of large scale structures in transonic jet mixing layer. *Proc. ASME FEDSM* 98-5234.

Ukeiley, L. S., Seiner, J. M. & Ponton, M. K. 1999 Azimuthal structure of an axisymmetric jet mixing layer. *Proc. ASME FEDSM* 99-7252.

Walker, S. H. & Thomas, F. O. 1997 Experiments characterizing nonlinear shear layer dynamics in a supersonic rectangular jet undergoing screech. *Phys. Fluids* **9**, 2562–2579.

Wänström, M., George, W. K. & Meyer, K.-E. 2005 POD applied to stereo PIV data of the far turbulent axisymmetric jet. *Bulletin of the 58th APS DFD meeting*., Chicago, IL.

Wygnanski, I. & Fiedler, H. 1969 Some measurements in the self-preserving jet. *J. Fluid Mech.* **38**, 577–612.

Zaman, K. B. M. Q. & Hussain, A. K. M. F. 1980 Vortex pairing in circular jet under controlled excitation. Part 1. General jet response. *J. Fluid Mech.* **101**, 449–492.

Zaman, K. B. M. Q. & Hussain, A. K. M. F. 1981 Turbulence supression in free shear flows by controlled excitation. *J. Fluid Mech.* **103**, 133–159.